Single molecule mechanics of biopolymers: An optical tweezers study

Joost van Mameren

September 20, 2002

Table of contents

Preface

This work describes the project I have done in the *Physics of Complex Systems* group at the Vrije Universiteit, Amsterdam, to obtain my degree as Master of Physics.

The project comprised micromechanical experiments on the semi-flexible biopolymers *microtubules* and *F-actin*. An independent measurement of the *flexural rigidity* of these filaments, i.e. their resistance against bending, is obtained. Apart from the decription and analysis of these particular experiments, a substantial part of this document is 'sacrificed' to describing experimental techniques applied in this work and, more generally, in our group.

I have tried to write mainly for two distinct audiences. First, I have tried throughout to enable my fellow students that chose other fields of physics for their master's projects, to understand what I have been working on—and why. Second, I hope that (future) students in our group—both M.Sc. and Ph.D.—will read this thesis as an introduction to the concepts and techniques that are applied in our group's research.

The thesis is divided into three parts. The first part introduces the (biological) context in which the experiments were performed (chapters 1 and 2). The model that was used to analyze the acquired data is presented (chapter 2) here as well. The second part describes the various experimental techniques—that of *optical trapping* (chapter 3), some microscopy techniques (chapter 4) and that of acousto-optic deflection (chapter 5)—ending with a description of our setup bundling these techniques. The last part lists the obtained results and compares them to both the here introduced model and the literature values. A few appendices should serve as a reference for the more technically interested reader.

Joost van Mameren
Amsterdam,
August 2002

Part I

INTRODUCTION

CHAPTER 1

Biological background

This chapter contains a (very) basic introduction to molecular biology. The content is focused on and constrained to motivating the experiments I did for this thesis, by characterizing their biological context.

1.1 Proteins

Proteins are one of the generic functional building blocks of life at the molecular level. They come in a wide variety of dimensions and functionalities, but share some general features that are addressed in this section.

Proteins consist of long chains of *amino acids*. Amino acids are made up of an amino group (–NH_2), a carboxyl group (–COOH) and a specific side chain, all bound to a carbon atom (figure 1.1a). Only twenty different types of these side chains are found in nature, each of which has its own size, shape, charge, hydrogen-bonding capacity and chemical reactivity.

Two amino acids covalently bind through their respective carboxyl and amino groups to form a *peptide bond* (figure 1.1b). Many amino acids joined via these bonds are called a polypeptide chain. A protein consists of one or

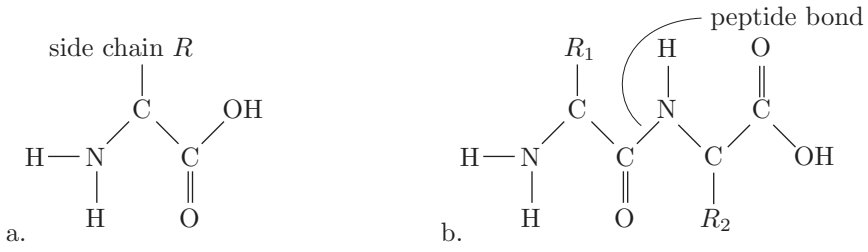

Figure 1.1: Generic structure of an amino acid (a), and two amino acids joined in a peptide bond (b).

more polypeptide chains, folded in a specific way that is determined mainly by the sequence of side chains of the comprising amino acids.

The architecture of proteins can be regarded on several levels of structure. First, there is the *primary structure*, which is the sequence of different amino acids of the polypeptide chain. This lowest level of structure determines all other levels and thereby the biological activity of the protein as a whole. The *secondary structure* describes the way in which the polypeptide chain is locally folded into regularly occurring stable structures like α *helices* and β *pleated sheets* (see figure 1.2). The *tertiary structure* describes the folding of these secondary structures into the final protein. Finally, the *quaternary structure* describes the way in which several polypeptide chains (or 'subunits') assemble into larger protein structures like, for example, dimers or tetramers. An example of a dimer is the protein *tubulin*, shown in figure 1.3.

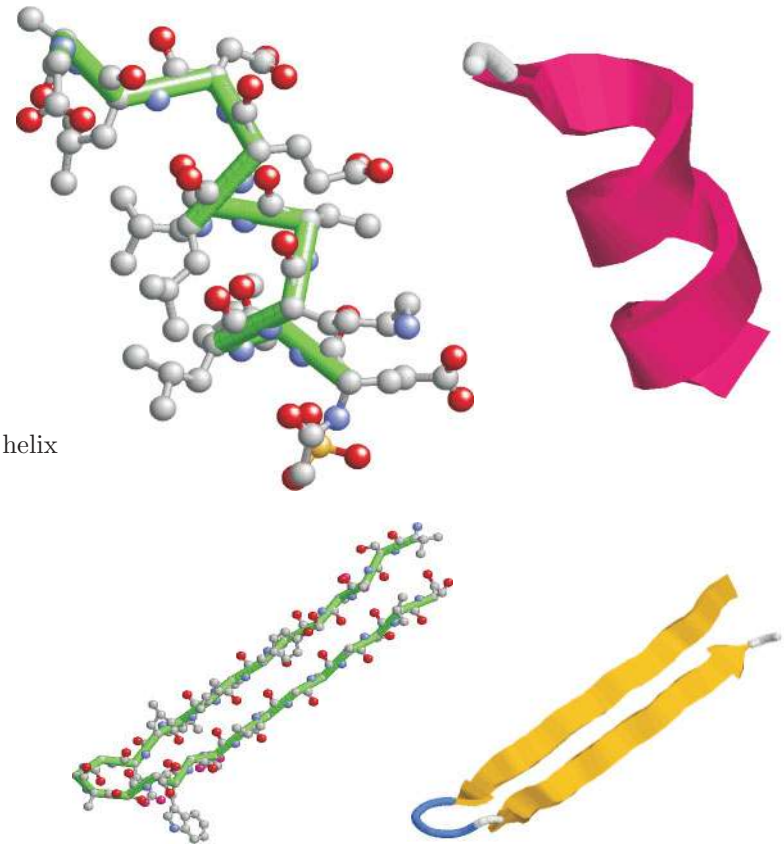

Figure 1.2: Structure of the α helix (top) and β sheet (bottom) recurring motifs. The figures on the left show the structures in atomic detail (polypeptide *backbone* is emphasized); the figures on the right depict their so-called ribbon diagrams, which are the standard representation in the literature.

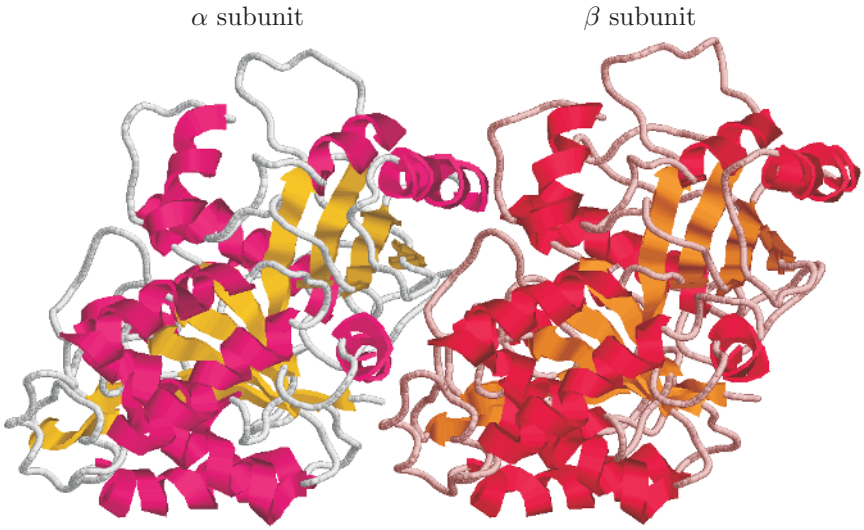

Figure 1.3: Structure of the dimeric protein tubulin, consisting of the two 50-kd subunits α and β tubulin. Tubulin is the constituent of the filamentous *microtubules*. (Structure taken from Nogales *et al.* [31].)

Proteins make up about 50% of the dry weight of biological matter, and play a central role in almost all biological processes. Their individual sizes can range from 50 to over 2000 amino acid units, which corresponds to a molecular weight ranging from 5.5 to 220 *kd* or *kilodaltons*[1].
Different proteins can have very diverse functionalities. Specific proteins called *enzymes* catalyze particular (bio)chemical reactions, increasing the corresponding reaction rates a millionfold or more. *Antibodies* are involved in the immunological defense of an organism. Some proteins are responsible for the regulated transport of chemicals through the organism (e.g. hemoglobin for oxygen transport). Motor proteins are able to convert chemical energy into mechanical energy, doing physical work (section 1.3). A last class of proteins I want to mention here are the ones that are part of the *cytoskeleton*, i.e. the set of molecules that help maintain the rigid mechanical shape of a cell (see section 1.2).

1.2 Eukaryotic cell structure

Living organisms can be divided into two fundamental categories according to their cellular organization. On the one hand we have the exclusively unicellular *prokaryotic organisms*, which have all their components (i.e. proteins and all

[1] A dalton is a mass unit identical to the atomic mass unit ($\frac{1}{12}$ of the weight of a carbon atom $= 1.66 \cdot 10^{-27}$ kg.

the machinery to make them) 'scrambled' together inside their cell membrane. Prokaryotic organisms originated as early as 3.5 billion years ago, which makes them the first life forms that appeared on Earth. They are typically not much larger than 1 to 2 μm. *Eukaryotic organisms*, on the other hand, have cells which consist of a nucleus and other compartments with specific functionalities, as well as a cytoskeleton that maintains the rigid cellular shape. Eukaryotic cells evolved 1.5 billion years ago and are typically 10 to 30 μm in diameter.

As the proteins addressed in this thesis are exclusively eukaryotic proteins, I will go into some more detail concerning eukaryotic cell structure. (This implies that occurrences of the word 'cell' refer to eukaryotic ones from this point.)

The most striking feature of the eukaryotic cell is its nucleus[2], which contains the genetic information of the entire organism in the form of long DNA molecules. Other compartments or *organelles* like the *mitochondrion*, *endoplasmic reticulum* and *Golgi-apparatus*, though typical components of the eukaryotic cell, will not be treated here. Instead, I want to focus on the structural scaffolding of the cell, the cytoskeleton.

The cytoskeleton consists mainly of two[3] types of polymeric protein filaments: *microtubules* and *actin filaments*, to be treated in the next two sections.

1.2.1 Microtubules

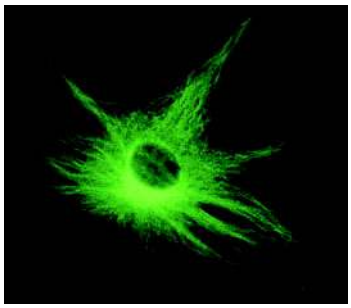

Figure 1.4: Fluorescently labeled microtubules in a cell.

Microtubules are rigid, tubular filaments of 25 nm diameter built from the dimeric protein *tubulin* (figure 1.3). Microtubules usually radiate outward from organelles near the nucleus called *centrosomes* (see figure 1.4). Apart from determining and maintaining the cell's shape, microtubules are also responsible for intracellular transport of organelles (section 1.3). They also play a key role in the dynamics of cell division (or *mitosis*).

The cylindrical nature of microtubules is shown in figure 1.5. One can see that the dimers line up to form a linear 'protofilament', thirteen of which align in a circular shape to form the tubular, hollow structure. The ordering of the α and β subunits in their protofilaments (together with their

[2]The word eukaryote stems from the Greek $\epsilon\upsilon$-$\kappa\alpha\rho\upsilon\sigma\tau\sigma\varsigma$ which means 'with a true nut', whereas the prefix $\pi\rho o$ in prokaryote means 'before', referring to its evolutionary appearance well before cellular nuclei.

[3]A third type, the *intermediate filament*, is not treated here.

intrinsic asymmetries; a protein never has a high degree of symmetry) defines a directionality along the long axis. This is why one distinguishes a '+ end' and a '– end' as the α and β subunit capped ends, respectively. This directionality comes into play when microtubules act as one-way tracks for motor proteins (see section 1.3).

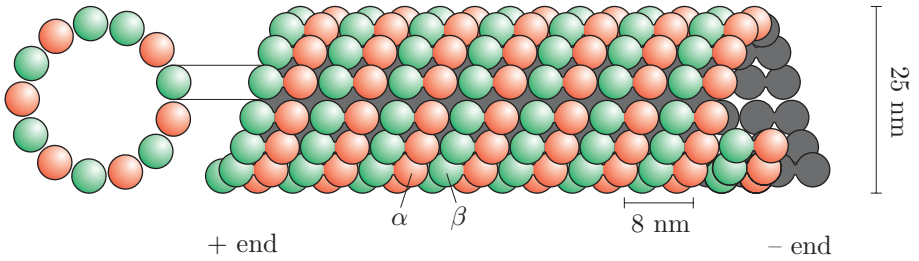

Figure 1.5: Schematic diagram of the helical structure of microtubules.

In a living cell, microtubules continuously polymerize and depolymerize at their end caps.In fact, this *dynamic instability* is exploited during mitosis, where the coordinated rapid assembly and disassembly are at the base of the physical separation of chromosomes into the two daughter cells.
The polymerization is coordinated by the *hydrolysis* (that is, decomposition by reaction with water) of the molecule *guanosine triphosphate* (GTP) into *guanosine diphosphate* (GDP), on release of a phosphate group. A polymerizing microtubule should have an end cap tubulin dimer that has GTP bound to it. Therefore, if the hydrolysis of GTP on the end cap protein occurs faster than the polymerization—turning the end cap dimer into GDP-tubulin—the microtubule will instantaneously start to depolymerize. Microtubules can be stabilized by adding a reagent called *taxol* (an anticancer drug) which prevents them from depolymerizing.
For details on microtubules' dynamic instability, see for example Stryer [38], chapter 15.

1.2.2 Actin filaments

Like microtubules, actin filaments make up part of the cytoskeleton. Actin filaments are polymers of the 42-kd protein *actin* or *G-actin*, where G stands for 'globular'. Analogously, actin filaments are also known as F-actin, the F denoting 'filamentous' or 'fibrous'. Actin filaments are thinner (8 nm in diameter) and less rigid than microtubules. They are formed by a 71.5 nm pitch helix of two protofilaments of monomers wound around each other, as shown in figure 1.6.
Actin filaments play a central role in the contraction of muscles. As with

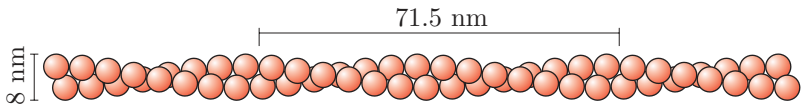

Figure 1.6: Schematic diagram of an actin filament.

microtubules, actin filaments act as one-way tracks for motor proteins, the unidirectionality being due to the monomers' intrinsic asymmetry. In muscle, contraction is caused by the cooperative pulling of motor protein filaments along actin filaments.

Analogously to microtubules, the polymerization process of actin is governed by ATP (*adenine triphosphate*) hydrolysis into ADP. In the case of actin, the critical concentration for polymerization is lower for ATP-actin than for ADP-actin.

1.3 Motor proteins

A specific class of proteins called *motor proteins* or *molecular motors* is responsible for doing physical work inside cells, e.g. directed transport of organelles, cell motility or contractile motion, the latter having macroscopic effects like the contraction of a muscle. In this section I will shortly address some general features of motor proteins, referring to the extensive literature for details (for example, Howard [24]).

1.3.1 Kinesin, myosin, ...

The proteins *kinesin* and *myosin* are motor proteins that do their work by binding to a microtubule or an actin filament, respectively, and dragging themselves along that track. This movement is unidirectional due to the intrinsic asymmetry of the track's building blocks, as was mentioned in the previous section. Kinesin and myosin are called *linear* motors, as they do their work along a linear track. In contrast, *rotary* motor proteins do their mechanical work by physically rotating some specialized part of the protein. For example, the bacterium *Escherichia coli* propels itself through its environment by rotating helical external *flagella*, driven by a rotary motor anchored in the cell membrane.

Kinesin is an elongated protein (360 kd, 110 nm long) consisting of a dimeric 'motor domain' that does the actual work, a tail which binds the cargo to be transported and a stalk formed by two tightly intertwined α-helices, con-

necting the two (see figure 1.7a). The motor domain consists of two identical heads, each with a binding site that can reversibly link to microtubules in a discrete way (i.e., with the tubulin dimers acting as localized binding sites). The *mechanochemical cycle* of the kinesin motor involves the hydrolysis of one ATP molecule per step. Some strains of kinesin are so-called *processive* motors, which means that they make many sequential steps along their tracks before detaching. The stepsize of a kinesin motor has been found to be 8 nm (in accordance with the $\alpha\beta$ dimer size; see figure 1.5), while a motor typically walks on a microtubule for several μm.

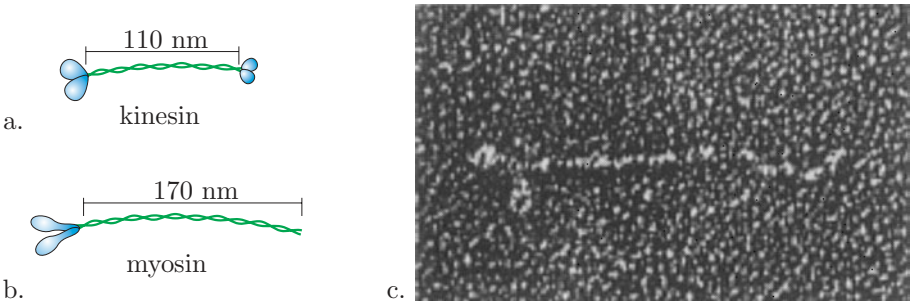

Figure 1.7: Schematic of a kinesin (a) and a myosin (b) motor protein (motor heads are on the left). Figure c shows an *electron micrograph* of a single myosin motor (from Elliott *et al.* [14]).

Myosin is a 520-kd motor protein which consists, like kinesin, of a dimeric motor domain and a long coiled α-helical stalk. The motor heads are connected by a flexible region, which may vary in length from one myosin strain to another. Most myosin strains are non-processive.Instead, myosin motors move along their actin tracks by application of single *power strokes* to them, upon which the motors release again. This makes them less suitable for the type of directed intracellular transport in which kinesin is involved. However, the cooperation of multiple myosin motors in muscle, assembled into so-called thick filaments, produce the directed motion that contracts the muscle at high speeds.

Besides kinesin and myosin there are more motors that act in a similar way. *Dynein* is a large protein that acts on, for instance, microtubules in assemblies called *axonemes*. Many dynein motors together are responsible for changing the overall shape of the axoneme, which forms the basis for the beating motion of a sperm cell's flagellum (see Stryer, [38]).

1.3.2 Motility assays

The motility of motor proteins is retained when extracted from the living cell and analyzed *in vitro*. This enables one to perform experiments to investigate the mechanical properties of motors with a wide range of experimental techniques.

One experiment which only takes a microscope capable to visualize the filaments (see chapter 6) is the *sliding assay*, shown in figure 1.9. Motors are attached to a microscope cover glass. Filaments floating in solution will be grabbed by the motors on the surface and dragged along in a linear fashion (provided there is sufficient ATP around). Depending on the processivity of the motors, the speed of the filaments depends strongly or not at all on the density of motors on the surface. Some typical video frames a myosin-actin sliding assay is shown in figure 1.8.

Another, more quantitatively applicable motor experiment is the *three-bead assay*, devised by Finer *et al.* [17]. A filament is suspended in between two micrometer sized beads, held in two independent *optical tweezers*. A third bead is immobilized on the surface and covered with motor proteins in low concentration. The action of a single motor protein can be observed by monitoring the response of the trapping laser light (see chapter 3). As will be described in section 2.4, in particular the three-bead assay motivates the experiments described in the following chapters.

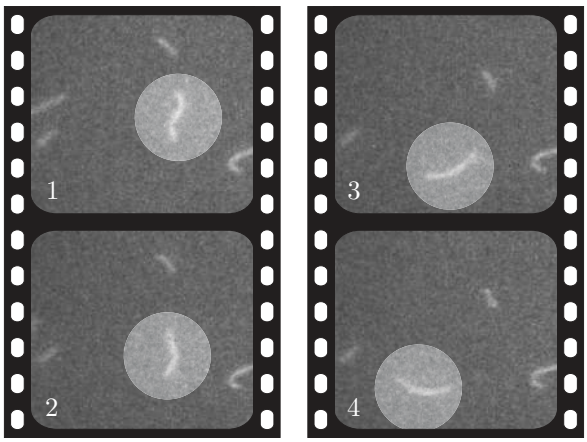

Figure 1.8: Inverted sliding assay with myosin motors and actin filaments. The highlighted filament obviously moves across the frames.

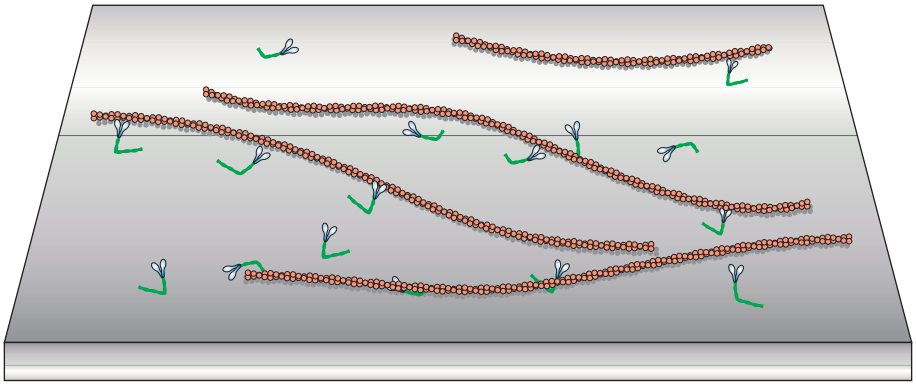

Figure 1.9: The inverted sliding assay, shown for myosin motors and an actin filament.

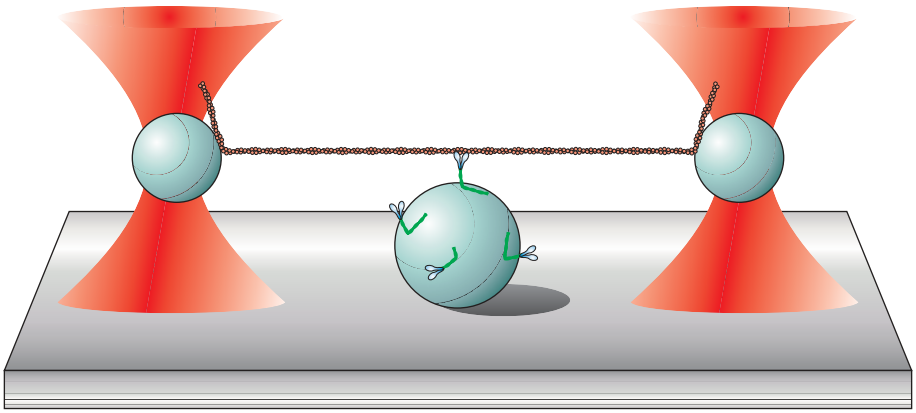

Figure 1.10: The three-bead assay, shown for myosin motors and an actin filament.

CHAPTER 2

Rigidity of semiflexible biopolymers

This chapter describes the basic scheme of the experiments I have performed to examine the rigidity of the semiflexible biopolymers microtubules and F-actin. For this purpose, the calculus needed for the analysis of the results is introduced.

2.1 The bent rod

How does a slender, rigid rod behave when bent by external forces? This question can be treated using freshman mechanics.

Consider a configuration as sketched in figure 2.1. A rod of length L is bent to have a (local) radius of curvature R. Due to the bending the upper, convex side of the rod is stretched along the length, whereas the lower, concave side is compressed. In between, there is a *neutral surface* which is neither stretched nor compressed. The amount of stretching or compression (that is, the ratio $d\ell/\ell$) is a function of the distance to the neutral surface y (see figure 2.1b):

$$\frac{d\ell}{\ell} = \sin\theta = \frac{y}{R} \tag{2.1}$$

According to *Hooke's law* (see [16]), the force per unit area in a small strip parallel to the neutral surface at a distance y is then

$$\frac{dF}{dA} = E\frac{y}{R}, \tag{2.2}$$

with E a proportionality constant called *Young's modulus*. For each compressive force below the neutral surface, there is an equal and opposite stretching force above it. These pairs of forces result in a torque or *bending moment* M around

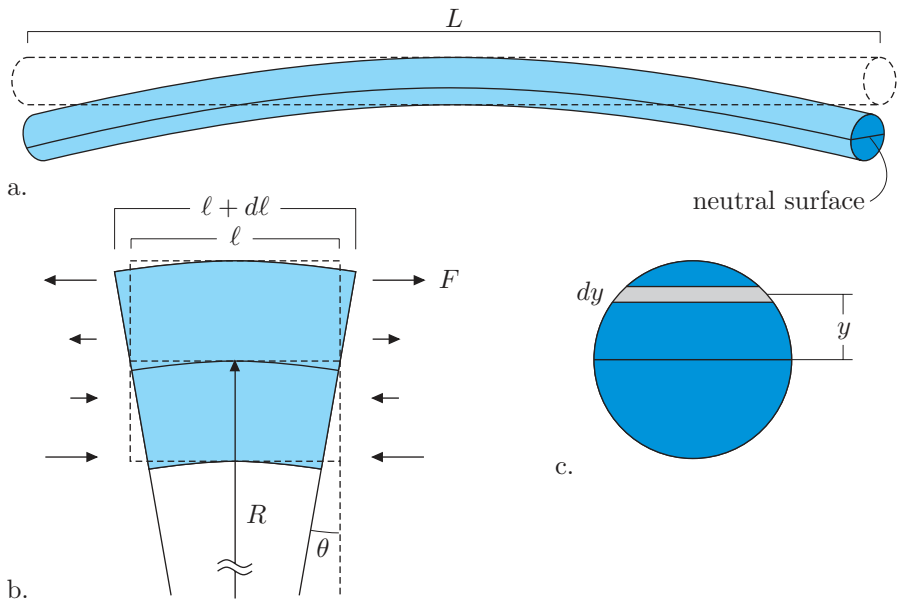

Figure 2.1: Geometry of a bent rod. Figure a shows the full length L of the rod. Figure b displays a small segment of the rod, showing forces increasing with the distance from the neutral surface. Figure c shows the rod's cross section with parameters y and dy. This figure was adapted from [16].

the neutral surface:

$$\begin{aligned} M &= \int_{\text{area}} y\, dF \\ &= \frac{E}{R} \int_{\text{area}} y^2\, dA \\ &\equiv \frac{EI}{R}, \end{aligned} \tag{2.3}$$

where I is called the 'bending moment of inertia'—analogous to the moment of inertia in rotating body mechanics. I is a measure for the distribution of matter around the neutral surface. The product of the material constant E and the 'shape factor' I, is called the bending stiffness or *flexural rigidity* EI. It is the rod's resistance to bending, just as stretching stiffness is the resistance to elongation. Equation 2.3 is called the *beam equation* (see [16]).

In general, the radius of curvature R may vary along the length of the rod. In order to incorporate that into the equations, we parameterize the rod with the variable $\theta(\ell)$, which is the angle of a segment of the rod at arc length ℓ with respect to some fixed axis. As can be seen from figure A.1b in appendix A, the curvature $1/R$ is then equal to $d\theta/d\ell$, giving for the beam equation

$$M(\ell) = EI \frac{d\theta}{d\ell}. \tag{2.4}$$

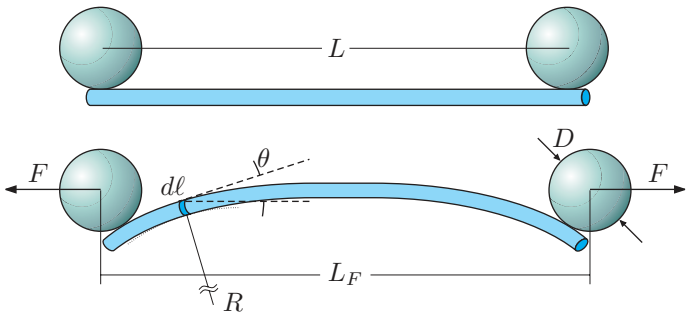

Figure 2.2: Configuration of a rod of length L bent by two laterally attached spheres of radius D, pulled apart by a force F along the line connecting their centers.

2.2 Bending experiments and model

Let us now consider the configuration shown in figure 2.2, which is the one of the bending experiments I performed on microtubules and actin filaments[1]. Here, the rod is bent by the moment generated by pulling apart two *laterally* attached spheres of diameter D. By applying the appropriate boundary conditions, the beam equation can be integrated once, as is done in appendix A. One finds:

$$\frac{d\theta}{d\ell} = \sqrt{\frac{F}{EI}\left(\mathcal{C} - 2\cos\theta\right)}, \tag{A.9}$$

with $\mathcal{C}$ a constant of integration. This equation can be numerically evaluated, as is explained in detail in appendix A. The results are shown in figure 2.3 for different values of the ratio L/D. The figure shows the (dimensionless) force versus the (dimensionless) extension X, which is the deviation ξ of the distance between the spheres at a force F from the relaxed distance L, divided by the sphere diameter:

$$X \equiv \frac{\xi}{D} = \frac{L_F - L}{D}. \tag{2.5}$$

The force-extension behavior is highly nonlinear due to the lateral attachment of the spheres. Apart from the numerical analysis, approximations can be made to equation A.9 for the various regimes that show up in figure 2.3. This is explicitly derived in appendix A. An important result is the following formula, which is in excellent agreement (figure A.5 on page 85) with the numerical results for the intermediate and high extension regions in figure 2.3 where the curves with different L/D converge:

$$\sqrt{\frac{FD^2}{EI}} = \frac{8}{3}X + 2\left(2 - \sqrt{2}\right)\frac{X^2\sqrt{X}}{1 - X}. \tag{A.28}$$

[1] The *anti*symmetric case, i.e. with the spheres attached on opposite sides, gives the same results for the high and intermediate force regimes, see appendix A.

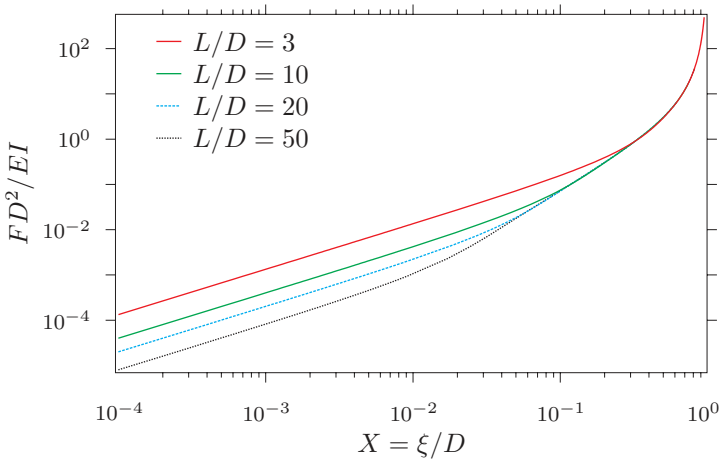

Figure 2.3: Numerical results of the bending equations. Curves are shown for different values of L/D with dimensionless force and extension variables. At higher extensions, the differences between curves with different L/D ratios disappear.

This force-extension relation can be used to fit experimental data, as will be done in chapter 7.

2.3 Flexural rigidity of microtubules and F-actin

The theory of the previous sections is used to analyze experiments in which micrometer sized beads are laterally attached to either microtubules or actin filaments and subsequently acted on by a periodic force pulling them apart. Distance and reaction force are recorded as a function of time. (These experiments are further denoted as *bending experiments*.) The fact that the beads are attached laterally and not on the end causes the filament to bend rather than extend—the stretch elasticity of these filaments is so much less than the effect of bending that is is entirely neglected in this analysis. This analysis should yield the respective values for the filament's EI as the single fit parameter. Various experiments have been performed in the past by laboratories around the world with the same goal, yet with divergent results—in particular for microtubules. I will discuss some of the experiments and results in chapter 8.

The experiments reported in the literature fall into two categories: the 'thermal' and the 'active' experiments. In the latter case, the filament's shape is mechanically disturbed while the response is recorded by some means—the bending experiments described in this thesis belong to this category. In thermal experiments one records fluctuations in shape due to the thermal bombardment of solvent molecules. These experiments require analysis in terms of statistical mechanics and polymer dynamics, using quantities like the thermal energy k_BT

and the *persistence length* L_p. The latter is mathematically defined as the characteristic length scale at which the tangent angle $\theta(\ell)$ becomes uncorrelated:

$$\langle \mathbf{x}(0) \cdot \mathbf{x}(\ell) \rangle \propto \langle \cos \Delta\theta(\ell) \rangle = e^{-\ell / L_p}, \tag{2.6}$$

where the first term is the time-averaged inner product of the direction vectors of two filament segments, separated by an arc length ℓ; $\Delta\theta(\ell)$ is the corresponding angle change (see figure 2.4). Intuitively, the persistence length is 'the length scale on which thermal bending becomes appreciable'; a floppy polymer like a DNA molecule has a shorter L_p ($\sim 10^{-8}$ m) than an actin filament ($\sim 10^{-5}$ m), which in turn has a shorter L_p than a microtubule ($\sim 10^{-2}$ m). Doi & Edwards [12] derive from this implicit definition the connection between these 'thermal' quantities and the mechanical quantity EI:

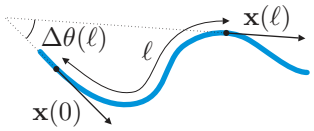

Figure 2.4: Parameters for persistence length definition.

$$L_p = \frac{EI}{k_B T}, \tag{2.7}$$

with k_B Boltzmann's constant and T the temperature. A polymer is called *semiflexible* if its persistence length is much larger than the monomer size (or the filament diameter), which is the case for actin and microtubules. A 'thermal' experiment could be the measurement of the mean squared end-to-end lengths of filaments, which vary due to thermal fluctuations, but are limited by the persistence length (see [24]):

$$\langle R^2 \rangle = 2L_p^2 \left\{ \exp\left(-\frac{L}{L_p}\right) - 1 + \frac{L}{L_p} \right\}.$$

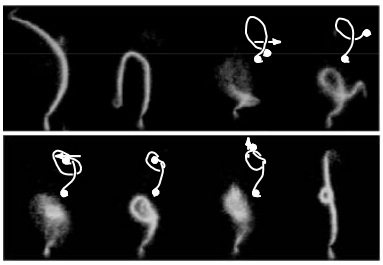

Figure 2.5: Consecutive stages of tying a knot in a single actin filament. Figure taken from [4].

Another experiment to determine the persistence length is the analysis of fluctuations in filament shape in terms of thermal modes, as was done by Gittes *et al.* (see [19]).

'Active' experiments often utilize *optical tweezers*—treated in chapter 3—or other experimental tools like micropipettes to actively manipulate the filaments. A nice example of a 'macho' experiment which does so is shown in figure 2.5, where micrometer sized beads are connected to a filament and manipulated to tie a knot in the filament.

2.4 Motivation for bending experiments

As described in section 1.2, filamentous actin and microtubules make up a large part of the cytoskeleton of the eukaryotic cell, maintaining the cell's shape by producing rigidity. Moreover, they are involved in physiological processes in which their stiffness is crucial: the appearance as tracks for motor proteins. Therefore, quantitative knowledge about their elastic properties is important in order to investigate their contribution to these processes.

Apart from yielding new and independent measures for the flexural rigidity of biopolymers, the bending experiments are also motivated by a technical issue, relevant for another experiment: a bead-filament-bead construct as shown in figure 2.2 is also the basis of the three-bead motility assay described in section 1.3.2 (see figure 1.10 on page 11). In these experiments, the bead displacements created by the motor protein on the filament are *attenuated* by the various compliances in the construct. The compliance of the bead-filament attachment is supposedly influenced to a large extent by the lateral attachment of the beads. Veigel *et al.* [42] have described these components in a qualitative way by treating the three-bead assay as a set of coupled springs, each with their own stiffness (the reciprocal of compliance), as shown in figure 2.6. Now, when a motor protein is pulling on the filament, this can be observed in force recordings on the bead only if the bead-filament attachment is stiff enough. This means that the construct needs to be put under tension. Knowledge about the (nonlinear) connection stiffness as a function of filament tension can be used to prepare the construct for optimal response to motor activity. The bending experiments will enable one to obtain this relation, by analysis of (the derivative of) curves like those in figure 2.3, yielding the stiffness $\kappa_{\mathrm{conn}} = dF/dX$ as a function of tension F.

After inspection of the model results for the force-extension behavior, it is expected that actin filaments, although being a lot more flexible than microtubules, reach a certain stiffness for lower tensions compared to microtubules, as they should get to the highly nonlinear part of figure 2.3 well before microtubules do.

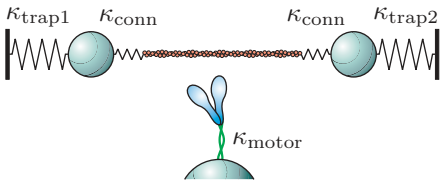

Figure 2.6: The three-bead assay in terms of the spring constants involved.

Part II

EXPERIMENTAL TECHNIQUES AND PROCEDURES

CHAPTER 3

Optical trapping

In this chapter, I introduce the technique of trapping microscopic objects with a focused laser beam.

3.1 Optical trapping theory

Just like matter particles, light quanta or *photons* carry momentum p:

$$p = \frac{E}{c} = \frac{h}{\lambda}, \tag{3.1}$$

where $E = h\nu$ is the energy of a photon of frequency ν and wavelength λ. This momentum can be imparted to objects upon collision, which is called the *radiation pressure* on the object. For macroscopic objects, the radiation pressure exerted by typical light sources is many orders of magnitude too small to have any measurable effect. However, for objects of microscopic dimensions (< 100 μm) it can have considerable effects, as was observed by Ashkin [5] in 1970 for 0.59- to 2.68-μm latex spheres and a focused argon laser of $\lambda = 0.51$ μm and a few mW power. He found that the spheres were trapped in the focus.

A focused laser beam can be used to trap small objects in a three dimensional 'potential well'. One speaks of an *optical trap* or, more figuratively, of *optical tweezers*. The theoretical description of this effect depends on the size of the trapped objects. One speaks of the **ray optics regime** when the object's dimension d is much larger than the wavelength of the trapping light: $d \gg \lambda$. In this case, diffraction effects can be neglected and the trapping forces of the light can be understood in terms of geometric or ray optics. The regime with $d \ll \lambda$ is called the **Rayleigh regime**. In that case one needs a description based on electromagnetic dipoles.

Unfortunately, in many practical cases micrometer-sized particles are trapped using visible or near infrared light of similar wavelength, which calls for an

approximative approach between the two above limits to obtain a quantitative estimate for the trapping forces. Nonetheless, I will give a short description of the two regimes to indicate the source of the optical trapping forces.

Svoboda and Block have written an excellent review article on the use of optical tweezers in biophysical research, including a review of the theoretical calculations in all size regimes. See reference [39].

3.1.1 Ray optics regime

In the ray optics regime the trapping force can be understood in terms of refraction of light rays between media with different indices of refraction (see references [5], [6], [7], and [8]). Figure 3.1 qualitatively depicts the origin of the trapping forces in this regime. The lateral gradient restoring force (figure 3.1a) can be understood as follows. If rays p_1 and p_2 come from parts of the beam with different intensity, the momentum changes of these rays (Δp_1 and Δp_2, respectively) differ in magnitude, causing a net reaction force on the refracting medium in the direction of highest intensity. The x-projection of this force, Δp_x, tends to counteract a displacement from the laser beam's axis.

The axial gradient force is also caused by momentum transfer upon refraction, resulting in a restoring force towards the focus, as can be seen in figures 3.1b and c. The figures do not take into account the fact that part of the incoming light is reflected rather than refracted—the scattering force. This light momentum reflection causes the object to be propelled out of the focus (along the light's $+z$-direction). The object is stably trapped if the scattering force along the $+z$-direction is compensated by the gradient force along the $-z$-direction.

Roosen and Imbert [36] have computed the optical forces on a dispersive sphere due to a light ray of power P, using the Fresnel reflection and transmission coefficients[1] R and T (see, for example, Hecht [23]). For the scattering force they found

$$\begin{aligned}\mathbf{F}_s &= \frac{n_1 P}{c}\left\{1 + R\cos 2\theta - T^2\frac{\cos(2\theta - 2\phi) + R\cos 2\theta}{1 + R^2 + 2R\cos 2\phi}\right\}\hat{\mathbf{u}}_{\parallel} \\ &\equiv \frac{n_1 P Q_s}{c}\hat{\mathbf{u}}_{\parallel},\end{aligned} \tag{3.2}$$

where n_1 is the index of refraction of the suspending medium, θ and ϕ the angles of incidence and refraction, c the speed of light and $\hat{\mathbf{u}}_{\parallel}$ a unit vector parallel to the incident ray. The term $n_1 P/c$ is the momentum per second of the light

[1] With this, the power of the fraction that is reflected immediately is PR; that of the doubly refracted rays in figure 3.1 PT^2, etc.

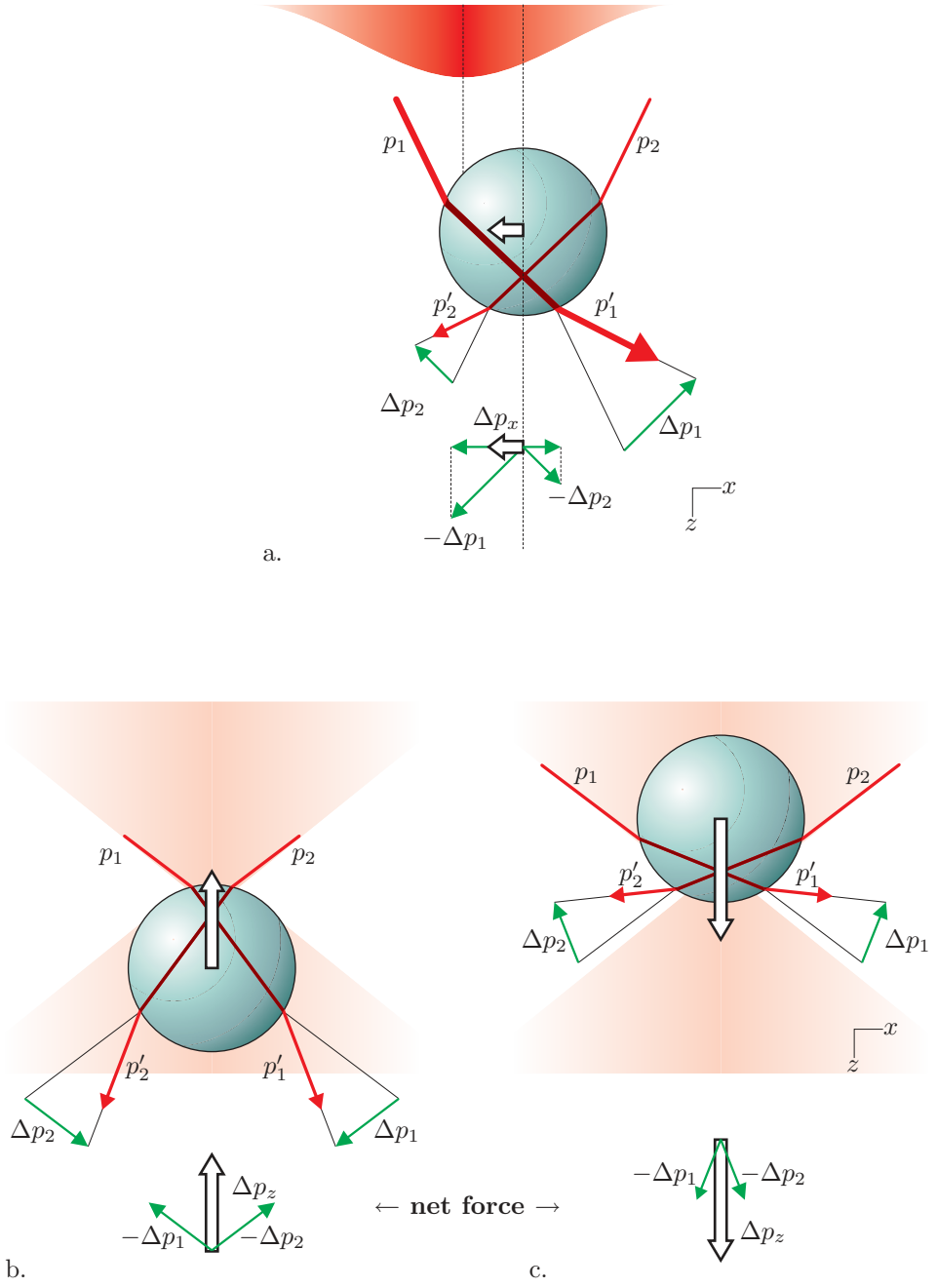

Figure 3.1: Qualitative picture of the origin of the trapping force. Figure a shows the lateral gradient force of a non-uniformly distributed laser beam. Figures b and c show the axial gradient force towards the focus of the trapping light. These figures do not show the scattering component due to *reflection* that tends to expel the object from the focus. The white arrows indicate the net restoring force in the respective directions; see text for details. (Figures adapted from Ashkin [6], [7].)

ray. The angle ϕ relates to θ via Snellius' refraction law: $\frac{n_2}{n_1} = \frac{\sin\theta}{\sin\phi}$, with n_2 the refractive index of the object.
Similarly, they found for the gradient force

$$\begin{aligned}\mathbf{F}_g &= \frac{n_1 P}{c}\left\{R\sin 2\theta - T^2\frac{\sin(2\theta-2\phi)+R\sin 2\theta}{1+R^2+2R\cos 2\phi}\right\}\hat{\mathbf{u}}_\perp \\ &\equiv \frac{n_1 P Q_g}{c}\hat{\mathbf{u}}_\perp.\end{aligned} \tag{3.3}$$

Vectorial addition of these two trapping force components gives for the magnitude of the force due to a *single* ray of power P:

$$F_{\text{tot}} = \frac{n_1 P}{c}\sqrt{Q_s^2+Q_g^2} \equiv \frac{n_1 P}{c}Q(\theta, \tfrac{n_2}{n_1}, R, T), \tag{3.4}$$

where the variables determining the effective Q-value have been explicitly stated. The total force on the object is found by summing over all rays passing through it. Ashkin has worked out these calculations for a laser beam with a Gaussian profile[2] [7].

3.1.2 Rayleigh regime

In the Rayleigh regime ($d \ll \lambda$), the trapped particles are treated as point dipoles, as the electromagnetic field is constant on the scale of the particle. The scattering force is given by

$$\mathbf{F}_s = n_1\frac{\langle\mathbf{S}\rangle\sigma}{c}, \tag{3.5}$$

where $\langle\mathbf{S}\rangle$ is the time-averaged Poynting vector of the electromagnetic wave and $\sigma = \sigma(d, \lambda, \frac{n2}{n1})$ the scattering cross section of a Rayleigh particle of diameter d.

The gradient force is the *Lorentz force* acting on the dipole induced by the electromagnetic wave:

$$\mathbf{F}_g = \frac{\alpha}{2}\boldsymbol{\nabla}\langle E^2\rangle, \tag{3.6}$$

where E is the electric field and $\alpha = \alpha(d^3, \frac{n2}{n1})$ the *polarizability* of the object.

3.1.3 Optimization of trapping power

From equations 3.2–3.4 it is obvious that—at least for the ray optics approach—the trapping forces can be enlarged by increasing the laser power P, the refractive index of the surrounding medium n_1, or the Q-values. The laser power can only be increased up to a certain limit, above which more laser light would lead to heating or photodamage of the optics or the examined system (often delicate biomaterials). Increasing the refractive index is hardly ever an option, as

[2] Often referred to as the 'TEM$_{00}$' mode of the laser.

most samples require an aqueous solvent of $n_1 \approx 1.3$. This leaves the geometric Q-values as the parameters to be optimized.

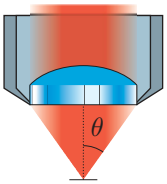

The maximum incidence angle $\theta_{\max}$ is determined by the optics used to focus the laser beam—usually and also in our case a microscope objective lens. One of the specifications of an objective is the so-called *numerical aperture* (or NA, see references [10], [23]). This is a measure for the solid angle over which the objective lens can gather light. It is defined as:

$$\mathrm{NA} = n_3 \sin\theta, \tag{3.7}$$

where n_3 is the refractive index of the *immersion medium* (i.e. the medium between the sample and the objective lens) and θ is one-half the angular aperture (see figure). The value of n_3 varies between 1.0 for air and ≈ 1.5 for most immersion oils. The NA of the objective in our setup is 1.3.

Another parameter which influences $\theta_{\max}$ in a similar way is the beam diameter d. As indicated in the figure, an expanded beam yields a larger $\theta_{\max}$ and therefore a stronger intensity gradient in the focus. To optimize the trapping quality with a Gaussian profile beam, the beam should *overfill* the back aperture of the objective lens. This increases the intensity of the highly convergent rays coming from the edge of the aperture compared to when the aperture is just filled. These convergent rays contribute largely to $\mathbf{F}_g$, enabling it to overcome the $+z$-scattering force.

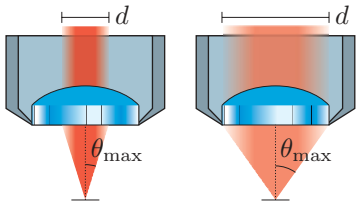

material	**index n_2**
silica (SiO_2)	1.37–1.47
polystyrene	1.57

Table 3.1: Refractive indices of common materials.

The refractive index of the trapped object n_2, or rather the relative index $\frac{n_2}{n_1}$ determines to a large extent how strongly the incident rays are refracted and, consequently, how strong the trapping force is. The required balance between gradient and scattering forces yields an optimal refractive index of $n_2 = 1.69$ (see [1], [39]). Table 3.1 lists the refractive indices of the most widely used materials. The table suggests that polystyrene (plastic) particles trap better than do silica (glass) particles, which is true provided the beam width is sufficiently expanded.

As was said before, neither the ray optics nor the Rayleigh approach is quantitatively applicable to practical applications, since the object's size and the wavelength of the trapping light are often of the same order of magnitude. In the case of our setup, the laser wavelength is $\lambda = 1.064$ μm, and the bead diameters for the experiments described here are either $d = 1.0$ or 2.17 μm.

However, quantitative physical experiments can still be performed with optical tweezers, as will be described in the next section.

3.2 Force detection

As was said in section 3.1, it is often hard to theoretically predict the force exerted by the trapping laser beam from first principles. It is possible, though, to use the trapping light that is scattered by the object to get an estimate for *additional* forces (i.e. other than the trapping force) acting upon the trapped object. These external forces tend to push or pull the object from the center of the trap. The refractive object, in turn, refracts the rays passing through it. Gittes and Schmidt [21] have developed a model based on far-field interference of the outgoing laser light with the scattered light from the trapped particle. This model describes intensity shifts due to the lateral (i.e. off-axis) displacement of the particle. The illuminating and scattered light is collimated by a *condenser* lens of focal length f. In the *back focal plane* (BFP) of this lens, the intensity distribution does not change when moving the optical trap around in the sample. The distribution is only affected by motion of the trapped object with respect to the trap. This is why this plane is imaged onto a *quadrant photodiode*—a light sensitive diode which is divided into four equal segments, which is used to detect changes in the intensity distribution. This method of displacement or force detection of a trapped object is known as *back-focal-plane interferometry*.

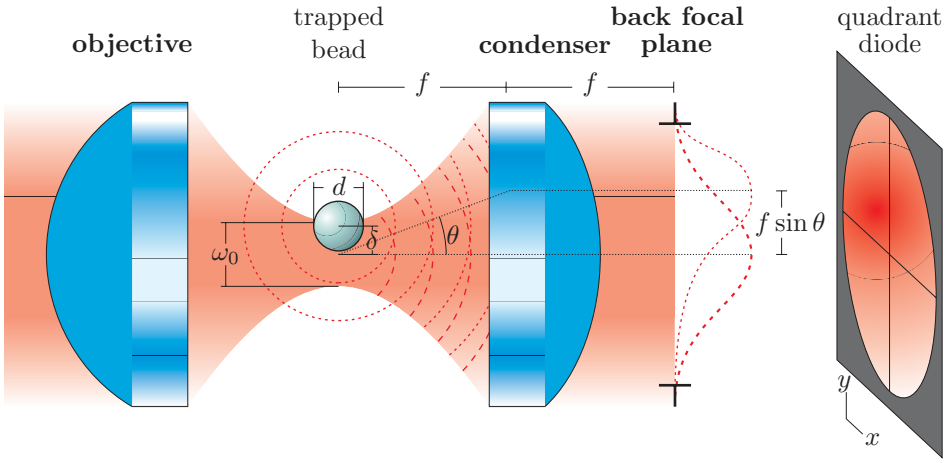

Figure 3.2: Configuration for the detection of lateral displacement of a trapped sphere from the trap center. The condenser's back focal plane is imaged onto a quadrant diode.

Figure 3.2 shows the configuration for the detection of the lateral displacement from the trap center. Figure 3.3 defines the intensity shifts in terms of the signals from the four segments of the quadrant diode. The following expression

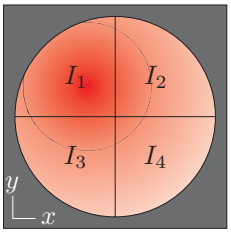

$$\left.\begin{aligned} I_{y+} &= I_1 + I_2 \\ I_{y-} &= I_3 + I_4 \end{aligned}\right\} D_y = \frac{I_{y+} - I_{y-}}{I_{y+} + I_{y-}}$$

$$\left.\begin{aligned} I_{x+} &= I_2 + I_4 \\ I_{x-} &= I_1 + I_3 \end{aligned}\right\} D_x = \frac{I_{x+} - I_{x-}}{I_{x+} + I_{x-}}$$

Figure 3.3: Intensity distribution signals D_x and D_y constructed from the light intensities I_j on the four individual segments of a quadrant photodiode.

can be derived for the detector response upon a displacement δ of a micrometer-sized spherical object, or *bead*, with diameter d from the center of a beam of focal waist diameter ω_0 (see [21]):

$$\begin{aligned} D_x = &\frac{I_{x+} - I_{x-}}{I_{x+} + I_{x-}} \approx 32\sqrt{\pi}\frac{n_1\alpha}{\lambda\omega_0^2}\,\mathcal{H}\left(\frac{\delta}{\omega_0}\right), \\ &\mathcal{H}(u) = \exp\left(-2u^2\right)\int_0^u \exp\left(t^2\right)dt, \end{aligned} \tag{3.8}$$

where the terms α and λ are, again, the susceptibility and the wavelength of the laser. The expression was derived in the Rayleigh approximation (see section 3.1), but has been found to quantitatively agree with the observed response also for particles in between the two regimes.

The response function from equation 3.8 is plotted in figure 3.4 for a 0.5 μm sphere diameter and a focal beam waist $\omega_0 = 0.53$ μm, which is the actual value for our objective and an unexpanded beam of 1.0 mm diameter. For small displacements ($|\delta| \lesssim 0.15$ μm), the response is approximately linear. The slope of the linear range scales with the bead diameter d as d^3, but its width is hardly affected by this parameter.

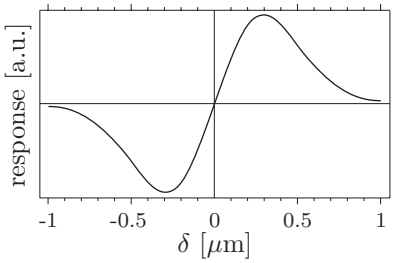

Figure 3.4: Detector response for $\omega_0 = 0.53$ μm and $d = 0.5$ μm.

If a force of known magnitude and direction is applied to the trapped bead (preferably within the linear range) and one observes the response of the quadrant diode signals, one can calibrate the detector to physically relevant units of force or displacement. This procedure will be treated in the next section.

3.3 Calibration of detector signals

3.3.1 Brownian motion and power spectra

As described in the last section, intensity shifts in the back focal plane of the condenser lens due to displacements of the trapped object from the trap center can be used to measure the forces causing these displacements. The detector response to external forces can be calibrated by applying forces of known magnitude to the trapped microsphere (bead). For instance, one can move the sample in which the trapped bead is suspended with constant velocity with respect to the position of the trap. The bead will be pulled out of the trap along with the sample motion due to the *viscous* or *Stokes' drag* of the fluid on the bead. When a fluid of viscosity η flows with velocity v along a bead of diameter d, the force on the bead is

$$F = 3\pi\eta dv = \gamma v, \tag{3.9}$$

where γ is called the drag coefficient.

Another, more accurate calibration procedure is to make use of the diffusional *Brownian motion* of the bead due to the continuous and random bombardment by solvent molecules. For a free bead, this bombardment gives rise to diffusion. After a time t, the mean square displacement of the spatial coordinate x will be (see [20], [34]):

$$\mathrm{Var}(x) = \left\langle x^2(t) - \langle x(t)\rangle^2 \right\rangle = \frac{2k_BT}{\gamma}t = 2Dt, \tag{3.10}$$

with D the diffusion constant, k_B Boltzmann's constant and T the temperature. Because of its temperature dependence, the Brownian force is also known as the thermal force.

A bead that is not free but held in an optical trap, will feel both the diffusional forces and a restoring optical force, confining its motion to within the laser focus. Assuming the confining force to be linear in the displacement with a proportionality constant κ, the *Langevin equation* (see [34]) for the bead's motion becomes

$$F(t) = \gamma\frac{dx}{dt} + \kappa x. \tag{3.11}$$

(Note that inertial forces have been neglected, which is valid since the *Reynolds number* $\mathfrak{R}$ is very low (10^{-4}) for micrometer sized objects.) $F(t)$ represents the random thermal force, which averages to zero over time. The *power spectrum* of $F(t)$, $S_F(f)$, contains the contribution to $F(t)$ of motions with different frequencies. For idealized Brownian motion this is 'white noise', i.e. the power

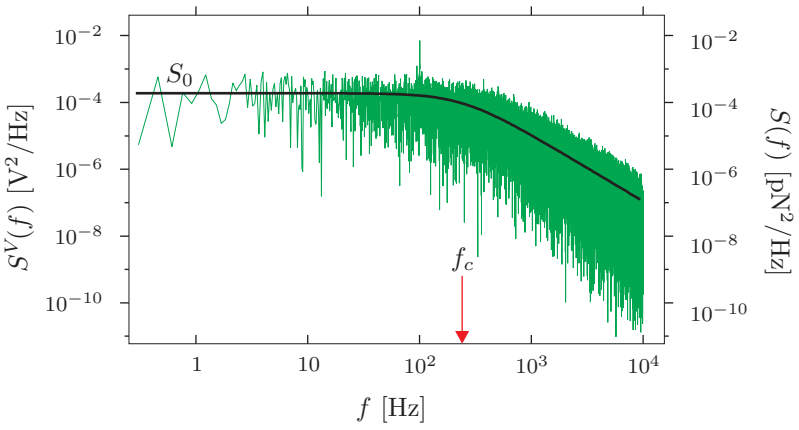

Figure 3.5: Typical power spectrum of a trapped bead. A 2.17 μm diameter polystyrene bead is held in a trap, while the D_x displacement signal (see section 3.2) is sampled at a 20 kHz rate. The low-frequency plateau S_0 and the corner frequency f_c are indicated. The left axis and the right axes correspond to the same spectra before and after unit conversion, respectively. The trap stiffness $\kappa = 0.03$ pN/nm.

spectrum is a constant (see [20]):

$$S_F(f) = |\mathcal{F}^2(f)| = 4\gamma k_B T, \tag{3.12}$$

where $\mathcal{F}(f)$ is the Fourier transform of $F(t)$. After calculating the Fourier transform of the Langevin equation 3.11—writing $\xi(f)$ as the Fourier transform for $x(t)$—and taking the modulus on both sides, the power spectrum of the displacement fluctuations is found to have a *Lorentzian* shape (see Gittes & Schmidt, [20]):

$$S_x(f) = |\xi^2(f)| = \frac{k_B T}{\gamma \pi^2 \left(f_c^2 + f^2\right)}. \tag{3.13}$$

Here, $f_c \equiv \kappa / 2\pi\gamma$ is introduced as a characteristic frequency of the trap. At frequencies $f \ll f_c$, the power spectrum is roughly constant, $S(f) = S_0 = 4\gamma k_B T/\kappa^2$. At $f \gg f_c$, it falls off like $1/f^2$. This is why f_c is known as the corner frequency. The high frequency behavior is characteristic of free diffusion, indicating that at short time scales the particle does not 'see' the confinement of the trap. A typical power spectrum is shown in figure 3.5.

3.3.2 Conversion to physical units

Once the values for S_0 and f_c are measured from fitting the observed displacement power spectrum of a trapped particle (see figure 3.5), these numbers can be used to find the trap stiffness κ:

$$\kappa = \frac{2k_B T}{\pi S_0 f_c} \qquad \text{or} \qquad \kappa = 2\pi\gamma f_c. \tag{3.14}$$

The stiffness κ has units [N/m], just like the spring constant in a mechanical spring.

It is important to note that the quadrant detector (section 3.2) reads the displacement fluctuations $x(t)$ as a voltage rather than a displacement in nanometers. The Stokes formula for the viscous drag coefficient on a bead ($\gamma = 3\pi\eta d$), which gives γ from first principles, can be used to calibrate the response R[m/V] of the detector if bead diameter and solvent viscosity are known:

$$R[\mathrm{m/V}] = \left[\frac{k_B T}{\pi^2 \gamma S_0^V f_c^2}\right]^{1/2} \overset{25^\circ\mathrm{C}}{=} \left[\frac{5.0 \cdot 10^{-20}\mathrm{m}^3/\mathrm{s}}{S_0^V f_c^2 d}\right]^{1/2}, \tag{3.15}$$

where a 25°C room temperature and the viscosity of water at that temperature have been substituted. The quantity S_0^V is the low-frequency limit of the power spectrum of the voltage data. To convert the data to forces, R should be multiplied by the trap stiffness[3] κ. Both the voltage data and the converted force data are shown in the two vertical axes of figure 3.5. Note that the power spectrum has 1/frequency units[4], which is due to the fact that the spectra are divided by their frequency resolution δf, to meet the normalization criterion

$$\sum_{i=1}^{N/2} S(f_i)\delta f = \left\langle x^2(t) - \langle x(t)\rangle^2 \right\rangle = \mathrm{Var}(x), \tag{3.16}$$

with N the number of samples (see Gittes and Schmidt, [20]).

[3] Compare to Hooke's law for a spring: $F = \kappa \Delta x$.

[4] The power spectrum is also called power spectral *density*.

CHAPTER 4

Microscopy techniques

This chapter describes two techniques to enhance the contrast and optical resolution of a microscope. The first one, *differential interference contrast* microscopy, employs differences in refractive index in the sample to generate contrast. The other, fluorescence microscopy, essentially makes selected objects in the sample luminesce.

4.1 DIC microscopy

The optical microscope section of the setup (chapter 6) is equipped for contrast enhancement and is able to resolve structures which cannot be resolved by ordinary bright-field microscopy.

The technique applied in our setup is called *differential interference contrast* (DIC) microscopy[1]. The arrangement of the optical components is shown in figure 4.1a. DIC is based on interference of two spatially separated, coherent light rays. These rays may follow paths of different optical length and hence can (constructively or destructively) interfere upon recombination.

First, the light is linearly polarized by a polarizer. Then the beam is physically split into two orthogonally polarized rays by a *Wollaston prism*. This prism consists of two wedge shaped birefringent[2] parts with mutually orthogonal optical axes (see figure 4.1b). A light ray at normal incidence, polarized at 45° with respect to both axes will be split in two at the interface between the wedges: the ordinary or *o*-ray in the first prism becomes an extraordinary or *e*-ray in the second and vice versa. Accordingly, they are refracted toward and from the interface normal, respectively. Note that this description applies to the 'original' Wollaston prism; in practice a *Nomarski-modified* Wollaston prism is

[1] Reference [10] has some illustrative Java-applets about DIC.

[2] See [23] for a description of birefringence.

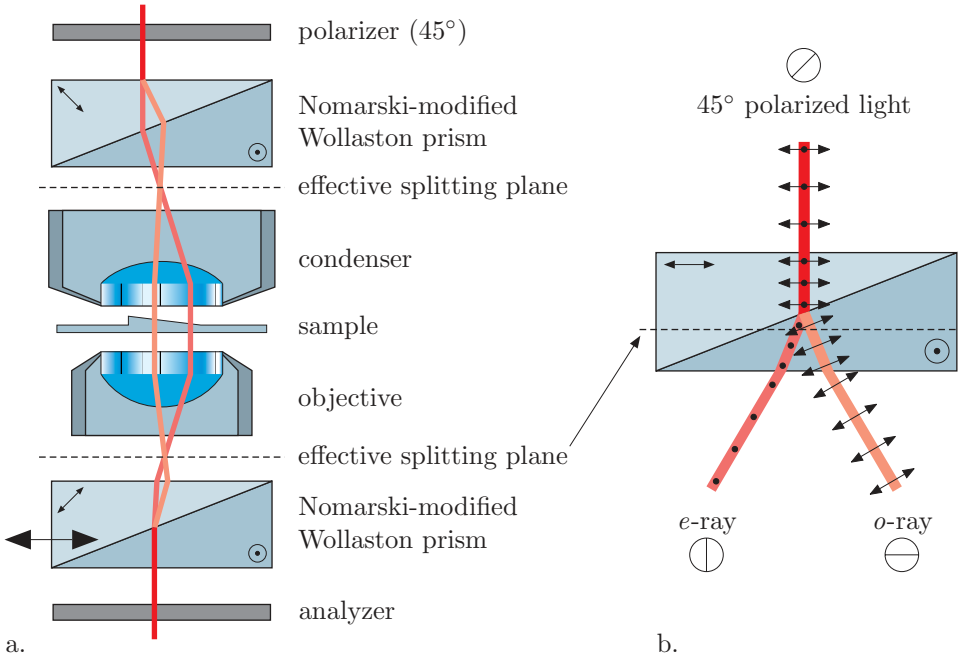

Figure 4.1: *Differential interference contrast* (DIC) implementation. Figure a shows the various components; figure b explains the beam separation performed by a Wollaston prism (unmodified)—input and output polarizations are indicated. See text for details.

utilized. This prism has the effective splitting plane moved well outside the prism (compare figures 4.1a and b) to place it in the back focal plane of the condenser and the objective—this implementation is known as Nomarski-DIC.

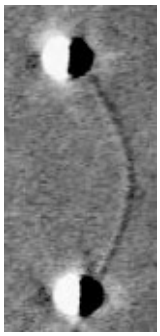

Figure 4.2: DIC image.

The slightly separated beams[3] subsequently pass through the condenser, the sample and the objective. In the sample, the now parallel rays follow slightly separated trajectories, encountering optically different structures—in particular, local changes in refractive index—which induce a phase offset between the two rays. After the objective, the two rays are brought together in a second Nomarski-modified Wollaston prism, which is mounted on a movable stage. These still orthogonally polarized rays are then made to interfere by projecting their polarizations onto the original direction in another polarizer called the *analyzer*. Depending on the phase offset between the two rays, the interference can be (partly) destructive, which shows up as a dark spot in the image.

An additional phase shift between the two rays can be added by laterally moving the second Wollaston prism. This can be exploited to control the image

[3]Typically, the separation ranges from 150 to 600 nm; see [10].

contrast by adding an offset light level. Microscopic objects visualized with DIC have one side appearing darker than the other, which creates the illusion of the picture being three dimensional. This is an optical effect that does not reflect the true geometric nature of the specimen. It should be noted that, although the DIC technique can visualize objects smaller than the optical resolution of the microscope, it does not provide spatial resolution below the diffraction limit ($\sim\lambda/2$). Therefore, the dimensions of structures may appear larger than they actually are. This is clearly seen in figure 4.2, which shows a 25 nm diameter microtubule (section 1.2.1) suspended between a couple of 1 μm beads.

4.2 Fluorescence microscopy

Another microscopy technique to visualize objects smaller than the optical resolution is *fluorescence microscopy*[4]. Fluorescence is the emission of light by a molecule, caused by the preceding absorption of light of *shorter* wavelength. The redshift of the fluorescent light can be exploited to spectrally block out the exciting light, such that the fluorescent molecules in the sample will be visible.

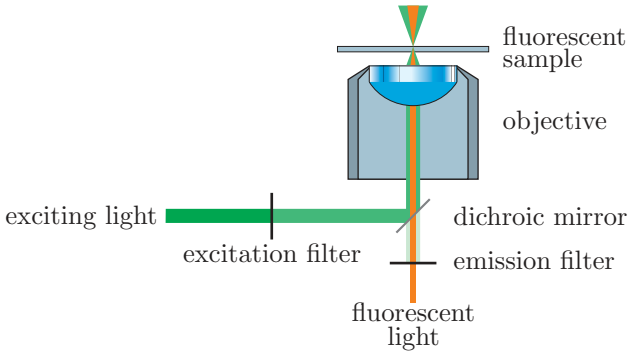

Figure 4.3: Components of an epi-fluorescence microscope. The excitation filter spectrally narrows the excitation light. A dichroic mirror couples this light into the objective lens. The objective collects the backwards emitted fluorescence light. The emission filter blocks out all but the emission wavelengths.

A typical configuration is shown in figure 4.3. To avoid spectral overlap, the excitation light source is filtered by a narrow width bandpass *excitation* filter. A dichroic mirror, reflective for this wavelength, couples the light into a microscope objective lens. In the sample, fluorescent molecules absorb the excitation light, and subsequentially re-emit at a redshifted wavelength in all directions. In so-called *epi-fluorescence* microscopy, the objective collects the 'backwards' emitted fluorescence light. The dichroic mirror is largely transparent for this

[4]For a nice introduction on fluorescence and fluorescence microscopy, see [10].

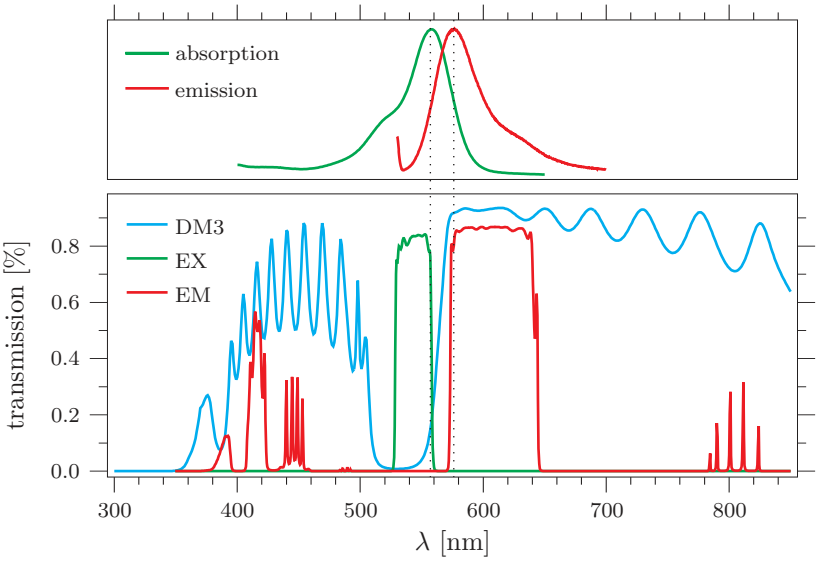

Figure 4.4: Top graph: absorption and emission characteristics of the fluorescent dye rhodamine (or, more specifically: *rhodamine phalloidin*). Bottom graph: transmission characteristics of the used fluorescence filter set (EX: excitation filter; DM: dichroic mirror; EM: emission filter). The absorption and emission maxima of the dye are indicated in both graphs. Data were taken from the company's websites, Molecular Probes (`http://www.probes.com`) and Chroma (`http://www.chroma.com`).

wavelength. A second bandpass filter—the emission filter—is used to filter out the remaining excitation light.

If the investigated specimen does not fluoresce naturally, a fluorescent *label* can be attached to it. For the bending experiments with actin (chapter 2), I have labeled non-fluorescent *actin filaments* (see section 1.2.2) with a fluorescent dye called *rhodamine phalloidin*. The biochemical procedures are described in appendix B.3. This molecule absorbs most at 557 nm, whereas the emission maximum is at 576 nm. The absorption and emission spectra of this dye, as well as the transmission characteristics of the filter set suitable for it, are shown in figure 4.4.

A typical image of a fluorescently labeled actin filament is shown in figure 4.5. The length of the filament is ≈ 10 μm. As with DIC microscopy, the width of the object (8 nm) appears exaggerated in the fluorescence image.

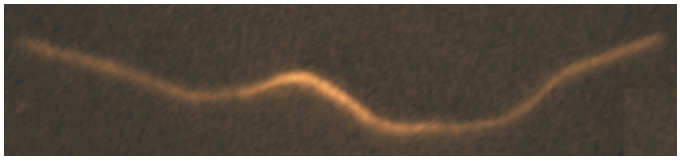

Figure 4.5: Actin filament labeled with the fluorescent dye rhodamine phalloidin.

CHAPTER 5

Acousto-optic deflection

This chapter describes the technique of acousto-optic deflection, used in our setup to implement computer controlled high resolution beam steering. Next, I describe the test experiments I performed for our set of AODs.

5.1 Principles of acousto-optic coupling

The elastic deformation of a solid body under strain causes a change of refractive index. This effect, upon which acousto-optic deflectors (*AODs*) are based, is called the *photo-elastic effect*.

Since an acoustic wave is nothing more than local compressions and expansions of the medium it is traveling through, an acoustic wave in a crystal will thus generate a periodically modulated refractive index. Electromagnetic waves can diffract on these, which is why the effect is alternatively designated the *acousto-optic effect*. An extensive description of this is given by Sapriel [37] and Xu [45], including all the cumbersome tensor notations needed for the general case of *anisotropic* crystals—with a different index in all crystal directions. I will outline the basic results described there, without reproducing derivations.

In a crystal with sound velocity v, a plane acoustic wave of frequency $f = \omega/2\pi$, wavelength $\Lambda = v/f$ and wave vector $\mathbf{K}$ (with $|\mathbf{K}| \equiv K = \omega/v$) will impose the following local variations to the refractive index n:

$$\delta n = \delta n_0 \sin(\omega t - \mathbf{K} \cdot \mathbf{r}). \tag{5.1}$$

This behaves like an optical grating of spacing Λ, traveling along its direction with a speed v. However, because of the speed of light being much larger, the grating can be considered static with respect to an incoming light beam. Figure 5.1 shows a typical configuration to illustrate the acousto-optic effect. An

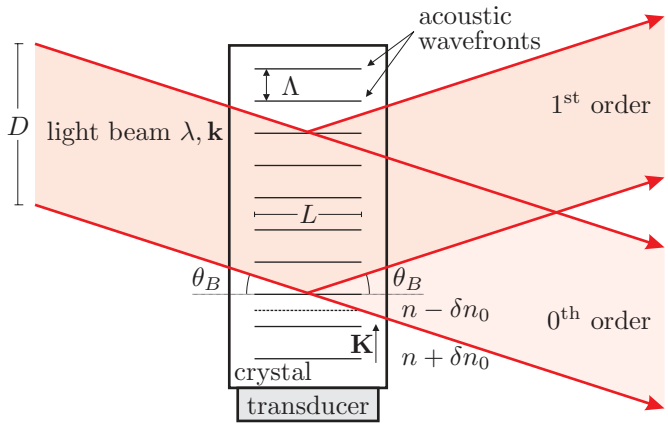

Figure 5.1: Light scattering off the wavefronts of a plane acoustic wave traveling through a crystal. The figure shows the case for *Bragg diffraction*, where the incidence angle should be the Bragg angle θ_B given by equation 5.3. The total beam deviation equals $2\theta_B$.

acoustic wave (usually in the radiofrequency region) is introduced in a crystal by a *piezoelectric* transducer, which converts an electric voltage to mechanical deformations (or vice versa).

An incident light beam (vacuum wavelength λ, wave vector $\mathbf{k} = \frac{2\pi}{\lambda}\hat{\mathbf{k}}$) diffracts on the acoustic wavefronts. Depending on the physical parameters of the configuration (light incidence angle, L, Λ, λ), two types of diffraction can occur. To distinguish, the following dimensionless parameter Q is often used:

$$Q = \frac{LK^2}{nk} = 2\pi\frac{\lambda L}{n\Lambda^2}. \tag{5.2}$$

For $Q \ll 1$, one speaks of *Raman-Nath diffraction*. The beam should enter the crystal at or near normal incidence. Diffraction in this mode is characterized by the generation of many diffracted beams of comparable intensities.This is mainly caused by the fact that the acousto-optic interaction length L is relatively small compared to the other length scales, such that out-of-phase diffracted light rays cannot destructively interfere[1].

The case with $Q \gg 1$ is known as *Bragg diffraction*. Here, only the first diffracted order is retained by constructive interference, provided the beam comes in at the *Bragg angle* θ_B:

$$\theta_B = \arcsin\frac{\lambda}{2n\Lambda} \approx \frac{\lambda}{2n\Lambda} = \frac{\lambda f}{2nv}. \tag{5.3}$$

The total deflected angle is equal to $2\theta_B$ (typically a few tenths of milliradians). Note that this angle is proportional to the acoustic frequency.

[1] Phase differences scale with the interaction length L—see reference [45], §2.3.

The diffraction efficiency η of the first order, i.e. the ratio of the first order diffracted to the incoming intensity, can be shown to be (see [45]):

$$\eta = \frac{I_1}{I} = \sin^2\left\{\frac{2.22}{\lambda}\sqrt{M_2 P_a \frac{L}{H}}\right\}, \tag{5.4}$$

where L/H is the length to height aspect ratio of the sound field, P_a the average energy flow or *acoustic power* (in J/s) and M_2 the acousto-optic *figure of merit*, which is completely determined by the crystal's material properties. For Bragg diffraction, the efficiency of the first diffracted order can be pushed to approach 100%. However, this only works for the ideal Bragg case of $Q \gg 1$. In practice, the interaction crystals are finite-sized ($\sim L$), which limits the Q-value. This implies that the higher orders are not fully suppressed. Moreover, if Bragg diffraction is used for beam steering by modification of the acoustic frequency/wavelength in an AOD, the Bragg angle for ideal operation changes (equation 5.3). Hence, the first-order efficiency decreases accordingly. Therefore diffraction efficiency has to be partly sacrificed for power stability of the deflected beam. It is possible to reduce this efficiency decrease by using *anisotropic* crystals, where diffraction efficiency can be stable over a relatively wide acoustic frequency band ($\lesssim$ one octave).

5.2 Testing and characterization

A set of orthogonal paratellurite (TeO_2) acousto-optic deflectors (model DTD-276HB6, IntraAction) was built into the experimental setup (shown in figure 6.1 on page 44) for beam-steering to manipulate the position of our optical trap in the sample. The AODs are shown in figure 5.2. The acoustic wave is generated by two piezo-electric transducers, which are driven by two independently programmable radiofrequency (RF) synthesizers, implemented on a PCI interface board. The RF electric signal is externally amplified. The interface board can be accessed and driven from within LabVIEW (or a lower-level programming language like C). The deviation of the first order diffracted beam with respect to the incoming beam is 45 ± 13 mrad ($47' \pm 13'$) for a 15 MHz amplitude sweep centered at 26 MHz. With the microscope optics as described in chapter 6, this translates to a displacement range of the (indirect) optical trap in the sample of 25.5 μm in the horizontal direction on the camera, and 25.7 μm in the vertical direction[2].

[2]The slight difference is due to the fact that the horizontally deflecting AOD—displacing the trap in the vertical direction on the camera—is located further away from the telescope lens and hence has a longer arm. See figure C.1 on page 91.

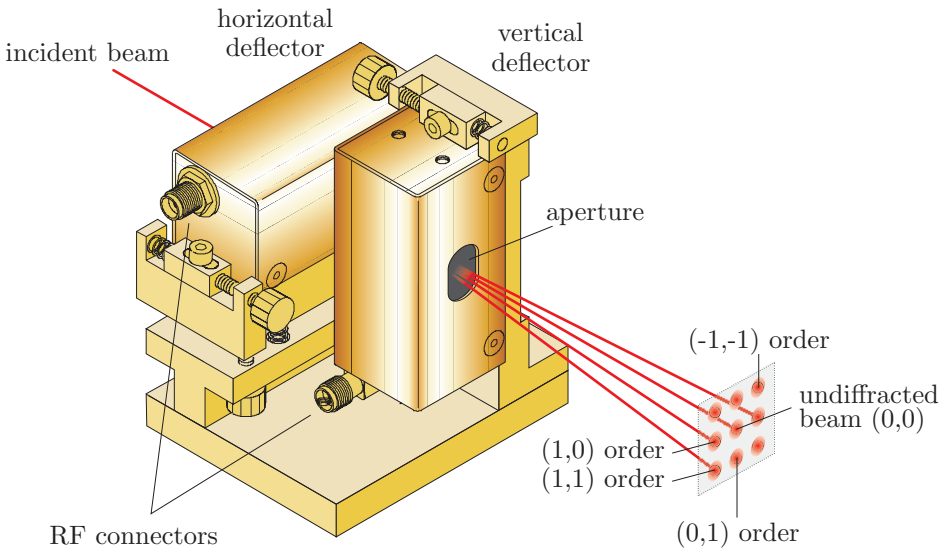

Figure 5.2: IntraAction TeO_2 AODs, model DTD-276HB6. The (1,1) diffraction order used for the laser trap is indicated, as well as some unused orders. The figure was adapted from the manufacturer's datasheet (`http://www.intraaction.com`).

As was described in the last section, the diffraction efficiency into the first order beam, η, is directly influenced by the acoustic frequency (equation 5.3). Hence, for use as a frequency controlled variable deflector, η should be measured as a function of frequency in order to yield a reasonably stable power in the deflected beam. In practice, this implies a trade-off between maximum efficiency and frequency stability.

This optimization was first performed with only the vertical deflector. The zeroth and first order diffracted beams were spatially separated and imaged on a set of photodiodes in such a way that the position on the photodiodes was fixed while scanning the acoustic frequency through more than an octave. Figure 5.3 shows the results of two scans from 10 to 40 MHz. The dashed line corresponds to the case where the AOD crystals alignment was optimized for maximum efficiency at 26 MHz acoustic frequency, pushing it to $\eta = 95\%$. The solid line shows the result of stability optimization. Clearly, η is stable from 18 to 34 MHz, but at the expense of a lower η value of $\sim$75%. For the latter case, the dotted line represents the sum of the undeflected and first order beam intensities. Dips in this curve indicate loss of light into other diffraction orders (-2, -1, 2, ...) due to imperfect Bragg diffraction.

A similar optimization procedure was performed for two consecutive AODs. In this case, the first AOD deflects the light in one direction and the second subsequently deflects the incoming beams in the perpendicular direction. Only one beam in the output 2D pattern of beams is used for x-y steering of the

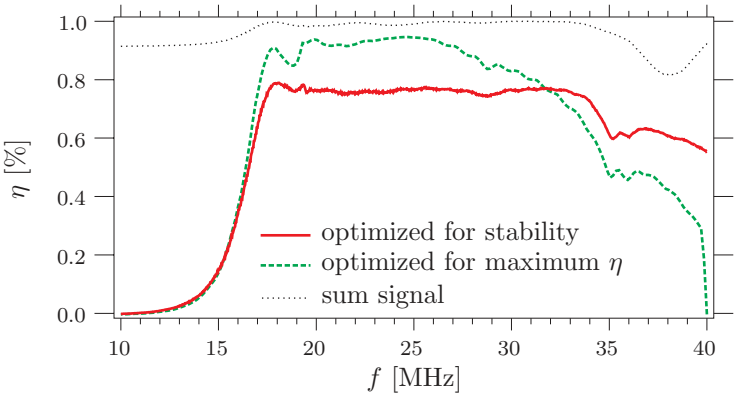

Figure 5.3: Diffraction efficiency η as a function of acoustic frequency f. The dashed line corresponds to the case where the alignment was optimized for maximum efficiency @ 26 MHz; the solid line is the result of optimization of stability over a one octave band. It is clear that the maximum efficiency is sacrificed for stability. As a control, the sum signal is shown (dotted curve) to monitor the loss into other diffraction orders.

optical trap (see chapter 6) and is optimized. This was performed by focusing four of the diffraction maxima onto the four segments of a quadrant photodiode: the undiffracted (0,0) beam, the (0,1) and (1,0) beams which are deflected only once and the final (1,1) beam—see figure 5.2. Figure 5.4 shows the optimization results of a scan from 10-40 MHz acoustic frequency at one deflector, while keeping the other frequency constant at 26 MHz. Note that the vertical axis now shows the total light intensity in the (1,1) diffraction order in arbitrary units rather than efficiencies in percents. The diffraction efficiencies η_{hor} and η_{vert} for both directions as follows:

$$\eta_{\text{hor}} \equiv \frac{(1,0)+(1,1)}{(1,0)+(1,1)+(0,0)} = 79\%, \tag{5.5}$$

$$\eta_{\text{vert}} \equiv \frac{(1,1)}{(1,0)+(1,1)} = 62\%. \tag{5.6}$$

The origin of these definitions should be obvious from figure 5.2; the values were obtained by averaging the quantities in equations 5.5 and 5.6 over the flat parts of the graphs in figure 5.4. Obviously, a change in deflection by the first AOD alters the angle of incidence at the second AOD, which is why the maximum overall efficiency with two consecutive AODs is lower than for one AOD. Up to 45% percent of all incoming light can be deflected into the (1,1) diffraction order over a reasonably wide frequency band.

Appendix C.2 describes the optimization as a part of the alignment procedure.

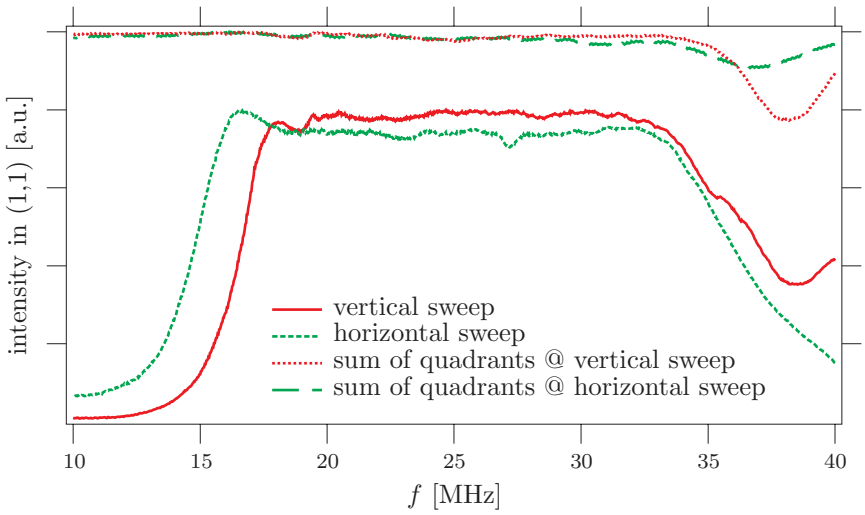

Figure 5.4: Intensities in the (1,1) diffraction orders as a function of acoustic frequency f during a vertical and horizontal sweep (solid and dashed lines, respectively). The AOD in the unchanged direction is driven by a 26 MHz frequency. Again, the sum signals of all quadrants are shown for monitoring the loss into higher diffraction orders, which obviously occurs for $f \gtrsim 33$ MHz.

5.3 Example of beam steering with AODs

As a nice illustration of what can be done with computer-controlled acousto-optic deflectors, I have implemented the well-known arcade game 'Pong', where a ball is being played between two paddles—see figure 5.5—into a C-program which drives the RF-synthesizers on the computer board (see last section). The result is shown in figure 5.6. The seven individual trap positions are time-shared with approximately 100 Hz frequency.

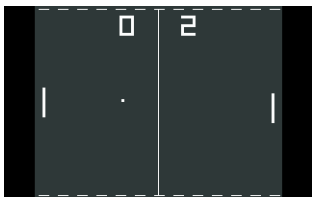

Figure 5.5: Screenshot of the evergreen arcade game 'Pong'.

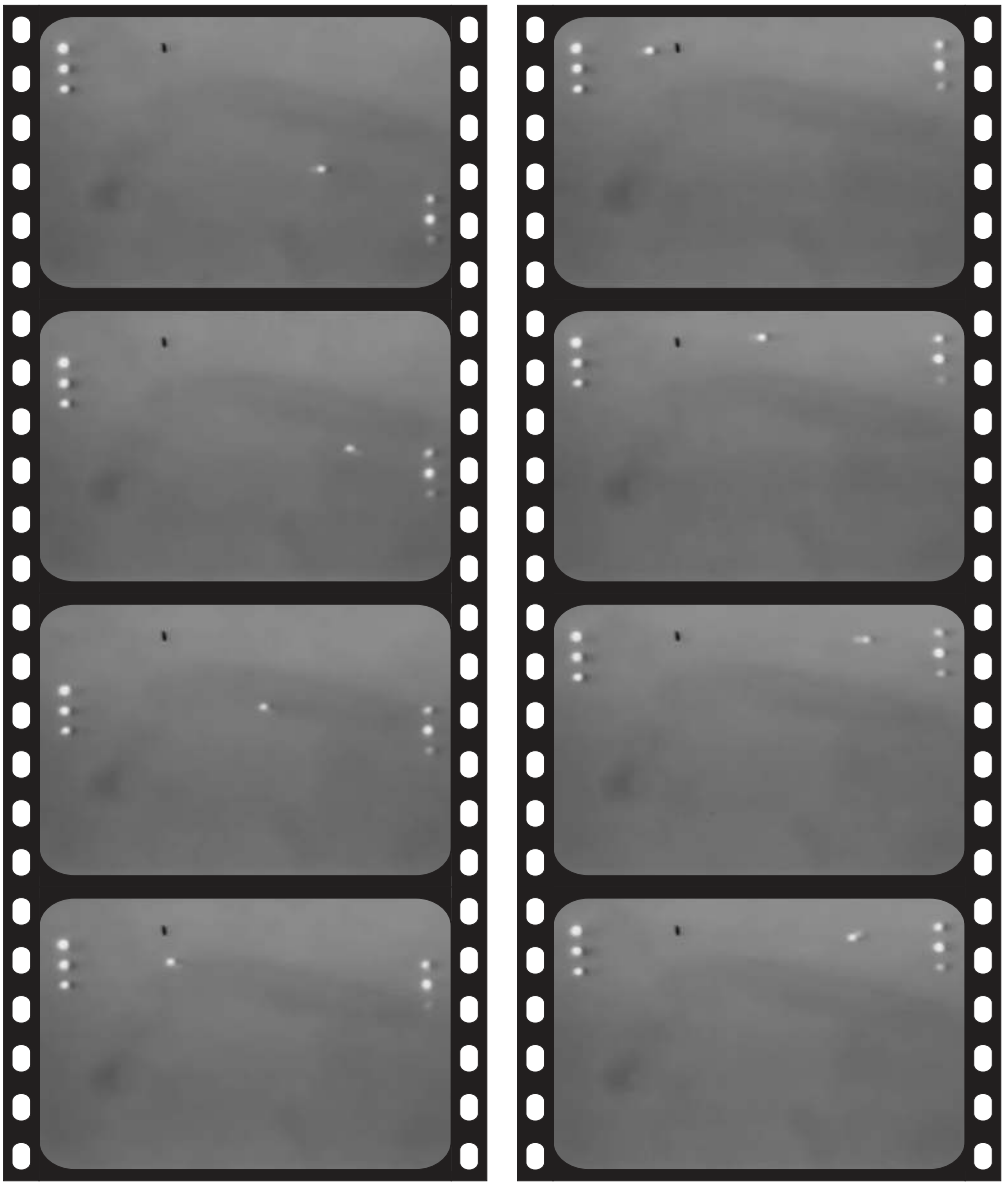

Figure 5.6: Pong implementation of some 0.5 μm silica beads, held by seven time-shared optical traps. Each pad consists of three trap positions.

CHAPTER 6

Experimental methods

This chapter introduces the experimental setup used to perform the bending experiments as introduced in chapter 2. Furthermore, experimental procedures for the bending experiments and the analysis of the acquired data are described.

6.1 Setup

The experimental setup used to perform the bending experiments consists of two partially overlapping lights paths: one for imaging the micrometer-sized beads and various biopolymers onto a camera, the other for the trapping laser light (see chapter 3). The setup is schematically shown in figure 6.1. Three parts can be distinguished, bounded in the figure by dashed lines.

6.1.1 Part I: trapping laser

Part I comprises the optics to control the laser beam for the trapping light. The linearly polarized beam from a Nd:YVO_4 continuous, diode pumped solid state laser[1] (1064 nm wavelength, 2 W maximum power, model Topaz 106C, Spectra Physics Lasers) is first expanded by a 3× beam expander (not shown) and then coupled onto a platform on our vibration isolating optical table by two mirrors M1 and M2, allowing for beam steering during alignment. The beam is further expanded by a second 3× beam expander (BE) to ≈ 10 mm in diameter.

The laser power is controlled by the combination of a rotatable half-wave plate ($\lambda/2$) and a polarizer. The wave plate rotates the linear input polarization, while only a fixed polarization passes through the polarizer. Hence, the laser power throughput can be tuned from 0 to 100%. Consequently, the laser can be run at constant, relatively high power for maximum stability.

[1] With a neodymium doped yttrium orthovanadate crystal as the lasing medium.

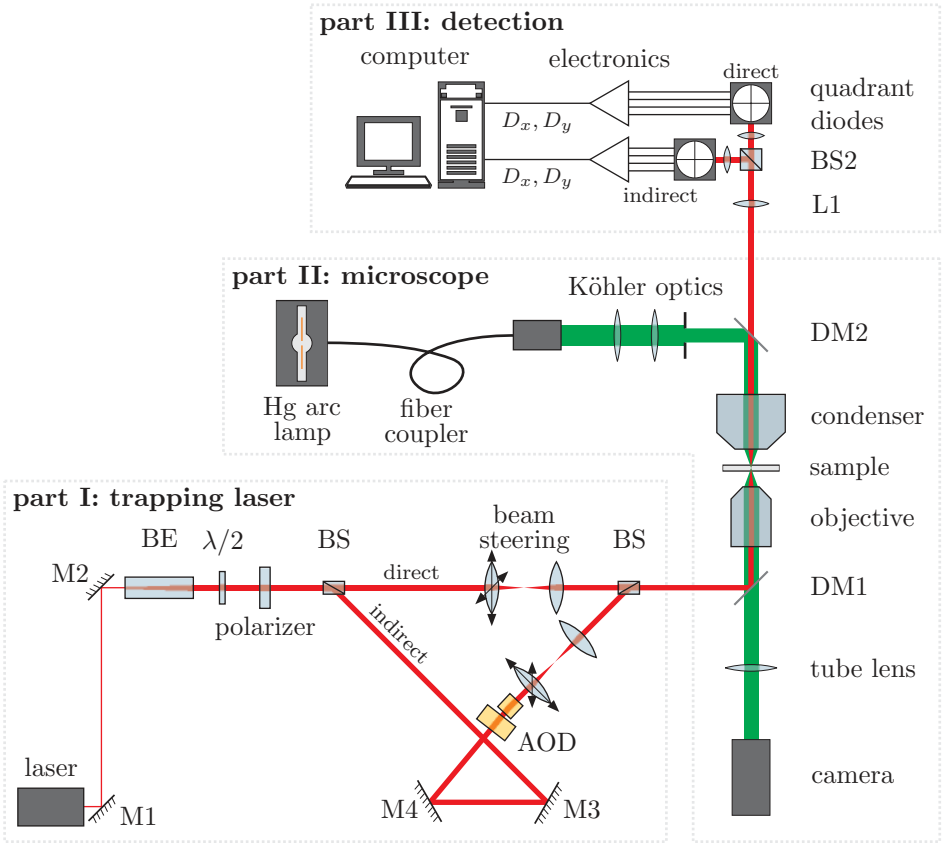

Figure 6.1: Schematic diagram of the setup. See text for details.

A Glan-Laser polarizing beam splitter (BS) splits the light in two perpendicularly polarized beams. These beams, the **direct** and **indirect** beams (see figure 6.1), will form two *independently adjustable* laser traps in the sample. The power ratio of the two beams depends on the input polarization and hence can be altered by changing the orientation of the polarizer.

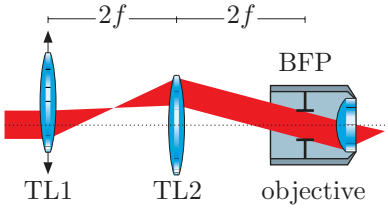

Figure 6.2: Telescope arrangement for trap positioning.

In both light paths a 1:1 telescope is placed which is used to change the position of the trap in the sample (figure 6.2). The second telescope lens (TL2) images the beam profile from the focal plane of the first telescope lens (TL1) onto the back focal plane (BFP) of the objective. A lateral displacement of TL1 causes the angle of the rays in the back focal plane to change, which displaces the lateral position of the focus in the sample plane. The *intensity distributions* in the objective BFP and in the conjugate condenser BFP remain unchanged.

In the path of the indirect beam, a set of acousto-optic deflectors (AODs)

is placed for additional computer-controlled high-resolution positioning of one of the laser traps (see chapter 5).

A second polarizing beam splitter is used to recombine the direct and indirect beams, which are then coupled into the microscope via a dichroic mirror (DM1).

The alignment procedure for this part and the detection optics (part III) is described in appendix C.

6.1.2 Part II: microscope

Apart from focusing the laser light to create the optical traps, the microscope is used as an optical microscope to form a highly magnified image of micrometer-sized structures in the sample.

The microscope can be used in either regular transmissive *bright-field* mode (shown in the figure and described here), in DIC mode (section 4.1) or in *epi-fluorescence* mode (section 4.2). All modes make use of *Köhler illumination* (described in great detail in reference [10]) with a 100 W mercury arc lamp, to ensure a uniformly illuminated microscope image.

The 545 nm line of a mercury arc lamp is selected with a line filter and coupled into a glass fiber. The use of a fiber facilitates switching the input position of the illuminating light between the aforementioned bright-field and epi-fluorescence modes (see below). A dichroic mirror DM2, transmitting the laser wavelength and reflecting the illuminating light, is used to couple the light into the microscope's core components: a 1.4-NA[2] oil immersion condenser lens (Zeiss), the sample and a 100× magnification, 'infinity-corrected', 1.3-NA oil immersion objective (Neofluor, Zeiss). The magnified microscope image is imaged onto an Ultricon tube camera (model VT1000, Dage-MTI). The camera has an external controller for analog gain and black level control. The analog video signal is digitized by a framegrabber computer board for digital contrast enhancement (e.g. background subtraction) and videotaped for off-line analysis of distances (see section 6.3).

Changing the focusing depth in the sample is accomplished by a motor which moves the condenser and objective lenses up and down with respect to the fixed sample. This is necessary for DIC microscopy (section 4.1), which strongly depends on the objective–condenser distance.

To modify the setup for *epi-fluorescence* microscopy, the illuminating light

[2] Numerical aperture, see section 3.1.3.

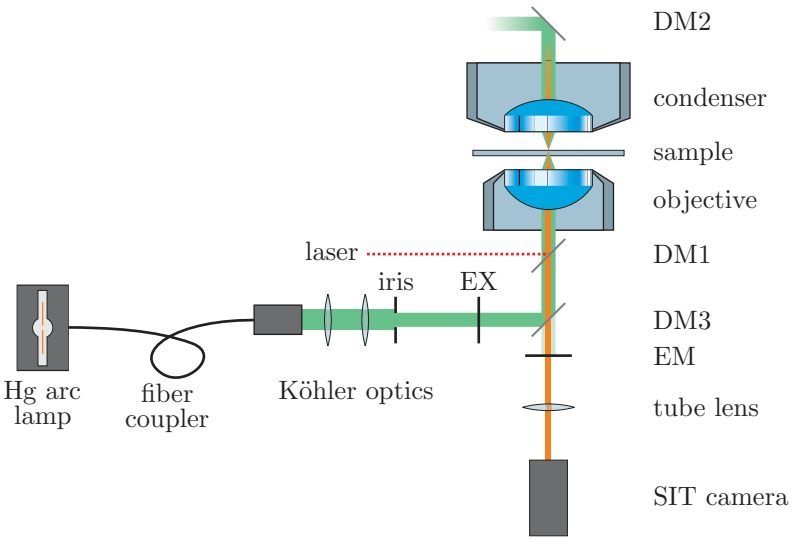

Figure 6.3: The setup of figure 6.1 changed to fluorescence mode. (DIC components are omitted.) New components are the exciter filter (EX), another dichroic mirror (DM3) and the emitter filter (EM). For clarity, the trapping laser is left out—only the mirror where it couples in is shown. See text for details.

should be inserted *below* the objective by moving the fiber coupler. Figure 6.3 shows how fluorescence imaging is attained. A third dichroic mirror (DM3) is used to couple the excitation light into the microscope. The green 545 nm line of the mercury arc lamp is selected by an excitation bandpass filter (EX) and coupled into the objective lens to excite fluorophores in the sample. The backwards emitted fluorescence light is collected by the objective and selected by an emission bandpass filter (EM), and imaged onto a SIT[3] camera (model VT1000 SIT, Dage-MTI), sensitive to the low light levels encountered in fluorescence microscopy.

Apart from the DIC and fluorescence optics, I have set up another light source to very faintly illuminate the sample in bright-field mode (via dichroic mirror DM2) while still exciting fluorophores in the samples and collecting the fluorescence light. By this, I was able to visualize both non-fluorescing microspheres (beads) and fluorescently labeled actin simultaneously.

This was achieved by introducing an iris in the path of the extra light source, positioned slightly *off-axis* such that with the smallest opening no light comes through. By gradually opening the iris, a tunable amount of bright-field light could be used to illuminate the non-fluorescent objects in the sample.

[3]SIT: silicon intensified target.

6.1.3 Part III: detection optics

The trapping light, transmitted by dichroic mirror DM2 and collimated by lens L1, is split by another polarizing beam splitter (BS2) to separate the orthogonally polarized direct and indirect beams. As described in section 3.2 and shown in figure 6.4, the light distribution in the condenser's back focal plane (BFP) is imaged by another lens onto two quadrant photodiodes—one for the direct and one for the indirect beam. Four each quadrant diode, the four pho-

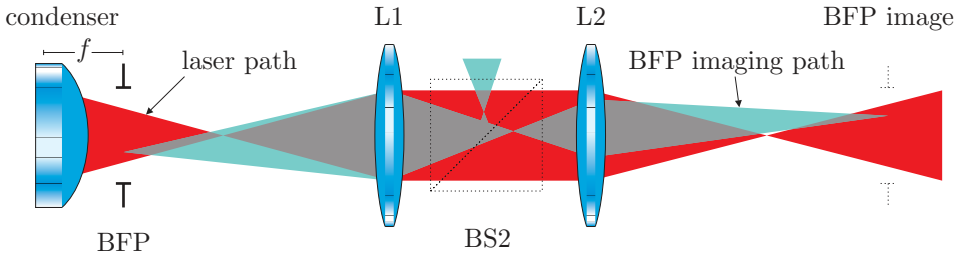

Figure 6.4: Back focal plane image formation.

tocurrent signals are converted to voltages, amplified and combined by analog electronic circuits to yield signals D_x and D_y, corresponding to the intensity distributions for the two lateral directions x and y in the back focal plane (see section 3.2).

It is important to note that although the DIC optics induces polarization changes, it does not or hardly interfere with the back-focal-plane interferometry detection. The polarization of both trapping beams is parallel to one of the two optical axes of the Wollaston prisms and hence these beams are not split like the illuminating DIC light[4].

The four displacement signals are sampled by a 16-bit analog-to-digital (A/D) converter PCI computer board (ChicoPlus board with AD16 A/D module, Innovative Integration). This board exploits a sampling technique called sigma-delta (Σ-Δ) conversion, which severely *oversamples* the input channels. This makes the use of anti-alias filters as described in reference [20] unnecessary. The digitized data is displayed by a custom-made LabVIEW[5] data acquisition application and saved to disk for off-line analysis (see section 6.4).

It is important to note that the use of AODs, which perform beam steering by deflecting the laser beam (see chapter 5) around a point which is not exactly imaged onto the BFP of the objective, introduce an artificial signal on the

[4]Note: the two DIC polarizers are situated outside the laser path and do not affect the trapping light.

[5]See `http://www.ni.com/labview`.

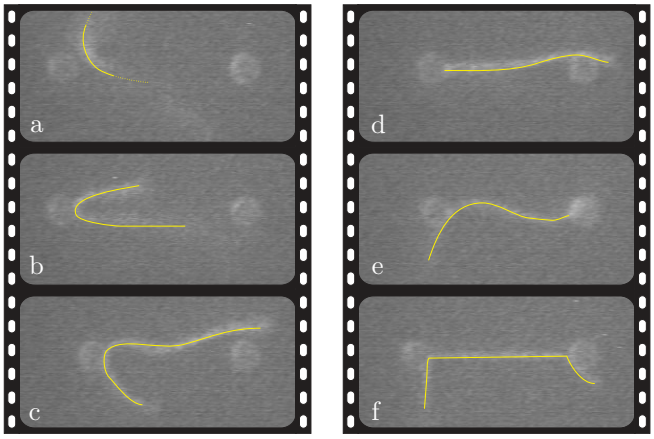

Figure 6.5: The preparatory stages of the bending experiments, shown for 2 μm beads and a fluorescently labeled actin filament (highlighted for clarity). See text for details.

quadrant diodes when the trap is moved. Hence, I have decided not to use the detector signals from the indirect trap to do force measurements.

6.2 Experimental procedure

As described in chapter 2, the main goal of the bending experiments is to find a relation between the force on the two laterally attached beads and the increase in distance between them due to that force. These are the parameters that are predicted by the bending model described in chapter 2 and appendix A. The flexural rigidity EI of the respective biopolymers can be obtained from a fit of the model to the data. Moreover, the force-extension behavior yields information about the compliance of the bead-filament-bead construct as a function of tension, as discussed in section 2.4.

A typical experiment comprised the following stages. First, a microscope sample chamber with beads and filaments was prepared as described in appendix B and inserted into the microscope. Depending on the type of filament, the microscope was set to either DIC or fluorescence mode, as explained in chapters 4 and 6. Actin filaments were fluorescently labeled; microtubules were not, yet can be seen nicely in DIC mode. Two beads were trapped by the direct and indirect laser tweezers. While keeping the trap positions constant, the microscope stage was moved in the x-y direction to bring a filament in the vicinity of one of the beads (figure 6.5a). As soon as the filament attached to a bead (figure 6.5b) via a biotin-streptavidin linkage (see appendix B.1), a viscous flow was generated towards the other bead by moving the microscope stage, in order to bring the filament in focus and close to the other trapped bead (figures 6.5c and d). After attachment to the second bead, the construct is ready for the experiment. This procedure typically took one to fifteen minutes. Figure 6.5f shows the construct

under relatively high tension, which can be seen from the sharp kinks at the connection points to the bead.

The experiments were carried out by *longitudinally* oscillating the AOD-steered (indirect) trap in either a sinusoidal or triangular wave manner, while recording three independent signals: the driving AOD frequency (which is a measure for the relative position of the trap; mainly used for control experiments), the quadrant diode signals of the two traps (see section 3.2) reflecting the external force on the beads and a video signal of the microscope image for (off-line) bead distance analysis (see section 6.3). Trap oscillation frequencies are sufficiently low to avoid effects of viscous drag on the bead or the filament: typically 0.1 Hz. By applying oscillatory pulling, the reproducibility of the measurements can be monitored. Moreover, potential variations over time can be observed. The amplitude of the oscillations is used to control the maximum pulling force.

On most occasions, the construct would break above a certain force. These events are obvious from both the force and distance (video) recordings as sudden jumps. Since these forces are well below the typical biotin-streptavin bond strengths ($\gtrsim$ 90 pN; see appendix B.1) connecting the filament to the beads, it is most likely that these breaks are caused by filament imperfections, which might be induced by photodamage due to the trapping laser light[6].

6.3 Video analysis

In order to use the video footage for quantitative determination of the distance between the slowly driven beads as a function of time during the oscillations, the video signal was first calibrated to convert pixels to real-world length scales. A microscope slide with a 10-μm scale division was used for this purpose. The video frames are digitized by a *framegrabber* computer board and processed by the 'IMAQ Vision' add-on package for LabVIEW[7]. A few algorithms are available to identify and measure objects in a digital image, to be treated in the next subsections. The required distance between the two bead centers was obtained as the distance between the centers of the two objects, found by either of the two algorithms.

[6] The use of *oxygen scavenging* chemicals (see appendix B) in the samples to reduce laser-induced photo-oxidation did not reduce the construct breaks.

[7] See `http://www.ni.com/imaq`. A nice conceptual introduction about the package is given in the *IMAQ Vision Concepts Manual* [30].

Figure 6.6: Blob analysis. The left image is a raw video frame (the actin filament is invisible due to photobleaching of the fluorophores). The right image is the result of thresholding and selecting for objects larger than 300 pixels. The calculated object centers and bounding boxes are indicated.

6.3.1 Blob analysis

Blob analysis is quite a rudimentary workhorse algorithm for digital image processing purposes. A blob—an acronym for **b**inary **l**arge **ob**ject—is acquired from a (greyscale) image by *thresholding* all pixels in the image higher than a certain grey value, yielding a binary (b/w) image. This image is then used to search for 'islands' of either black or white of user defined dimensions. These regions—the blobs—can now be evaluated for its physical properties like surface, 'center of mass', etc. Figure 6.6 shows an example of this strategy. Although easy to implement and use, the algorithm has the disadvantage of only taking into account information about object *edges*; a lot of information is discarded. This was in particular problematic with a DIC microscopy setting, where a bead appears as a bright and a dark semicircle (bottom image in figure 6.7 on the facing page), since blob analysis in that case only takes into account half of the real object's surface. During the bead tracking analysis required for the bending experiments, it was found that the blob analysis approach was only reproducible up to 0.5 μm.

6.3.2 Pattern matching

The technique of pattern matching is more sophisticated than that of blob analysis. It starts with a template image of the objects to be tracked, and calculates the *cross correlation* of this template image T with the image to be analyzed I:

$$C(i,j) = \sum_{n=0}^{N-1} \sum_{m=0}^{M-1} T(n,m) I(i+m, j+m), \tag{6.1}$$

where M and N are the pixel dimensions of the analyzed image. At the (i,j)-positions where a copy of the template object is actually located, the cross correlation will reach a maximum. The IMAQ Vision package incorporates some extensions to the (computationally expensive) cross correlating process, in order to reduce the amount of calculations. The most important extension is the

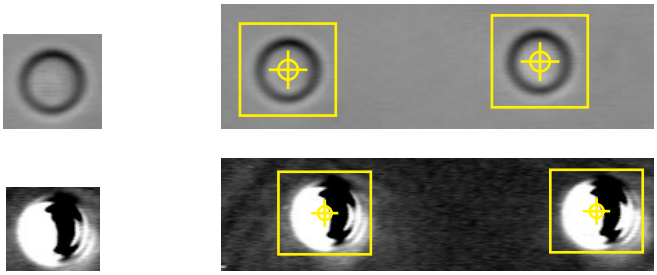

Figure 6.7: Two examples of pattern matching. The left images show the template image to be searched for; the right images show video frames and the found occurences of the template object. The bottom figure shows typical DIC images.

'interpretation' of the template image in terms of edges and other morphological features. Only around these features the full pixel content is used in the cross correlation; the other parts of the template image are taken along with a reduced pixel density, which reduces the effective amount of pixels used in the correlation process dramatically.

Contrary to blob analysis, the full pixel content of the template object is used for the search. Therefore, despite the higher computational efforts, this approach appeared to be more suitable for particle tracking. Reproducibility was found to be better than 0.02 μm by analyzing the same video frames multiple times. Only for video frames taken by the fluorescence camera, blob analysis was preferable to a template directed search because of the poorer signal to noise ratios due to the low light levels in fluorescence imaging (see the left image in figure 6.6).

6.4 Data analysis

The acquired data sets were processed as follows. First, the video footage was analyzed applying techniques described in section 6.3 to get the inter-bead distance as a function of time. Next, this distance data was synchronized with the force data (top graph in figure 6.8) by tuning the time offset of the video data. The distance data (acquired with *at most* the video rate of 25 Hz) was spline-interpolated (bottom graph in figure 6.8) in order to allow plotting high time-resolution force versus distance data in a scatter plot, eliminating time. In order to enable averaging of the interpolated data set over a user-defined number of samples, it was first sorted by ascending distance. Averaging was useful to reduce the brownian noise in the force data.

After these preparatory steps, the force-distance curve was ready for fitting to the model formula from the bending model as discussed in chapter 2 and in

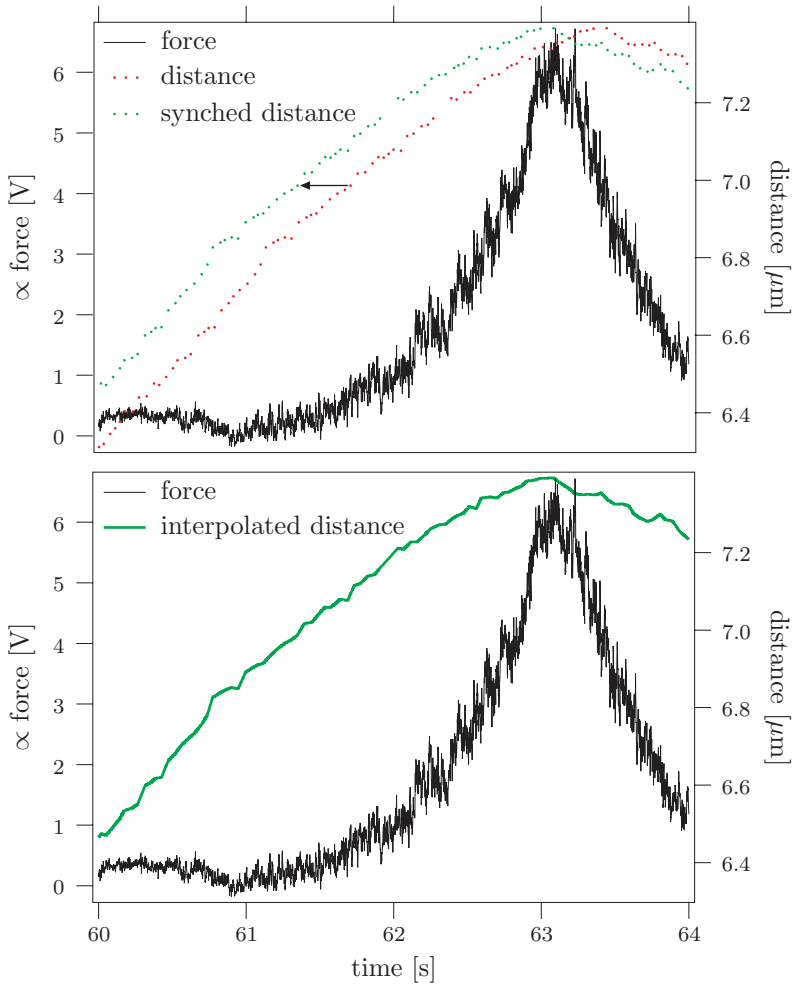

Figure 6.8: Preliminary steps in the data analysis. First, the inter-bead distance and pulling force data are synchronized (top figure) by tuning the time offset. Next, the distance is linearly interpolated to the sampling rate of the force data, to allow for a scatter plot of force versus distance (bottom figure). In addition, this new data set was sorted by ascending distances in order to facilitate averaging and fitting. Note that only a small segment of a typical data set is shown; typically three to ten of these oscillations were performed.

appendix A. For completeness, it is stated here in the form used for fitting the data:

$$F = \frac{EI}{D^2}\left[\frac{8}{3}X + 2\left(2-\sqrt{2}\right)\frac{X^2\sqrt{X}}{1-X}\right]^2, \tag{6.2}$$

with D the bead diameter and $X = (L_F - L)/D$ the (dimensionless) extension measured between the bead centers at a given force. For a given bead diameter and zero-force distance L, the flexural rigidity EI can be obtained as a fit parameter.

Before curve fitting, the following parameters are fixed:

- The offset of the force signal in volts—this parameter depends on the alignment of the quadrant diodes (see section 6.1.3);
- The force calibration factor (see section 3.3.2) to convert measured forces from volts to force units; this was obtained from a lorentzian fit to a power spectrum of the quadrant diode signal, taken at sample frequency of 15 kHz and up, *without* a connecting filament between the beads;
- The pixel calibration factor that converts the bead pixel distances, obtained from video analysis, to real-world length scales;
- An upper limit in the extension X to cut out the part of the data where the quadrant-diode force signal seems to run out of its linear response range (see figures 3.4 on page 27 and 6.9 below), appearing as a marked deviation from the steep increase;
- The (average) bead diameter D as indicated on the manufacturer's container—either 1.00 or 2.17 μm;
- The value of L, the distance between the bead centers in the relaxed case.

In particular the latter is difficult to determine experimentally, since the measured force is approximately zero over a relatively large range of distances—at distances where the filament is slack (figure 6.5e), the pushing force is too small to be measured, even for the relatively stiff microtubules (with L significantly larger than D). Therefore, experimental observation yielded L with a relatively large error. Eventually, L was incorporated in the *Levenberg-Marquardt* fitting routine. It is important to note that L cannot be used directly as a fit parameter during the fitting process, since the part of the data set which has $L_F < L$ (or $X < 0$) needs to be discarded to apply the fitting function from equation 6.2 above—only defined for extensions ($X > 0$). When L is used as a fit parameter, the range of data points that should be discarded is modified during execution of the fitting algorithm. If not, the algorithm will not converge. Therefore, a routine was written to fit the model formula to the data—with

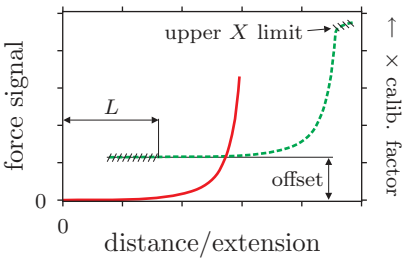

Figure 6.9: Parameters that are fixed while fitting. The dashed line shows the 'raw' data; the solid line is the processed data to which the model was fit.

EI as the single fit parameter—for incrementing values of L. The L-value that corresponds to the lowest value of χ^2 was used.

For both the synchronization and the fitting stage of the data analysis a separate LabVIEW program was written to automate the process.

Part III

RESULTS AND DISCUSSION

CHAPTER 7

Results

This chapter describes the results of the bending experiments performed on F-actin and microtubules.

7.1 Force-extension behavior

The bending experiment was performed ten times on microtubules and over twenty times on F-actin. The experimental parameters that were varied are the bead size D, the relaxed construct length L, and the laser power (that is, the trap stiffness). With the methods described in section 6.4, the time traces of the force signal from the quadrant diodes, sampled at 1 kHz, were synchronized with those of the distances between the bead centers (obtained from video analysis) and plotted against each other. Fixing a number of parameters (listed on page 53), the data was fit to the model equation 6.2 on page 52. The flexural rigidity EI was obtained from the fit.

During the analysis a significant number of data sets had to be rejected because of either one of the following issues:

- Multiple beads in one trap—in particular for 1-μm beads this was hard to detect during the experiment. The construct is modified due to this in an uncontrolled way. Moreover, the force calibration was done for one bead only;
- Irregularities in the force signal—for example, strong asymmetries in the slack region of the force signal with unknown origin;
- Suspicion of multiple filaments connecting the beads. In some cases, after the apparent occurence of a filament break (section 6.2), the connection turned out to be still present, indicating a multiple connection;

- Inferior video quality. Particularly footage from the fluorescence camera sometimes has an image quality which hampers reproducible particle tracking (see section 6.3). Moreover, the image formation onto the fluorescence camera turned out to be slightly distorted.

Five constructs with F-actin and two with microtubules were regarded suitable for analysis.

7.1.1 Typical fits results

Some typical fit results are shown in figure 7.1. The figure shows an actin data set and its best fit obtained from the procedure described in section 6.4.

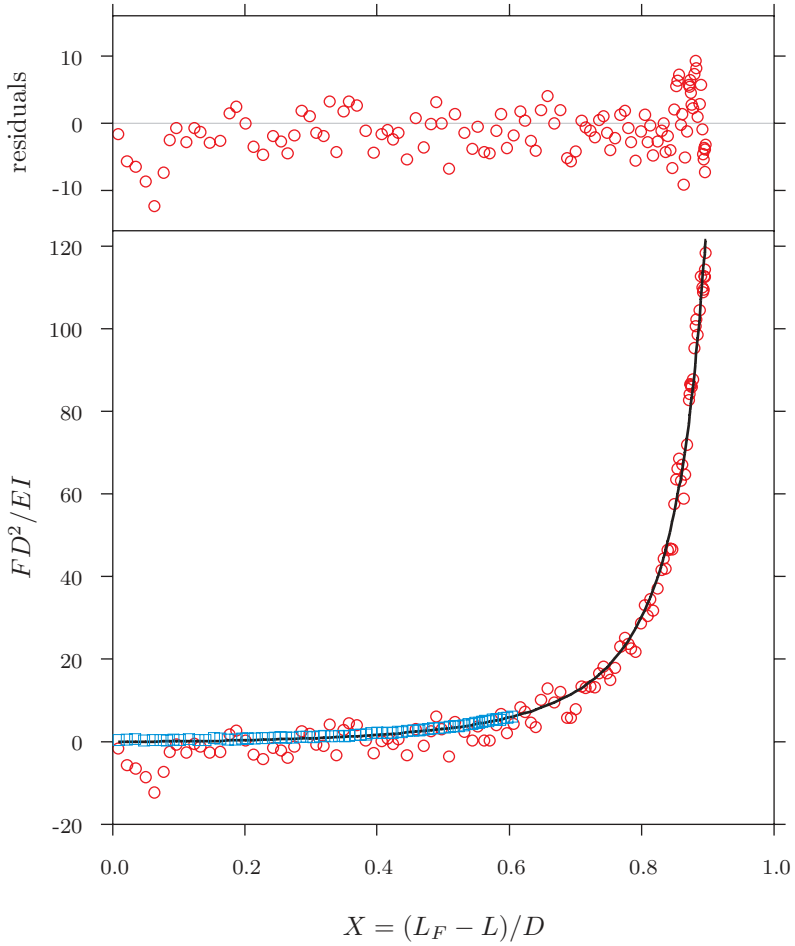

Figure 7.1: The bottom graph shows a normalized plot of the model equation 6.2, fit to a typical actin data set—data was averaged over 200 points. The squares represent a typical microtubule data set (fit not shown). The top graph shows the fit residuals (that is, data minus fit), which does not show significant features, suggesting that the data is well fitted by the model.

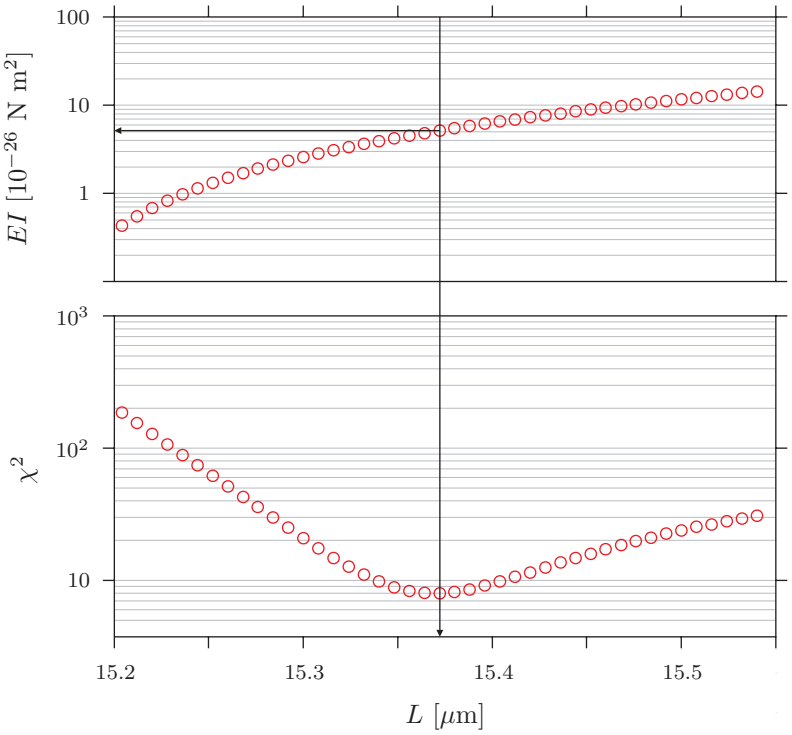

Figure 7.2: The optimal value for L in the fit of figure 7.1 was obtained by fitting the model with EI as the fit parameter, while stepwise incrementing L. The value of L corresponding to the lowest χ^2 (here: $L = 15.37$ μm) was selected; the top figure shows the corresponding EI value ($5.16 \cdot 10^{-26}$ N m^2).

The data is averaged over 200 points; the standard errors of these averages were used to weigh the data points. A microtubule data set is shown as well (squares). Note that it runs to considerably lower extensions for comparable maximum straining force, due to its higher rigidity. The top graph shows the corresponding residual values (data minus fit), which are randomly distributed around zero. This suggests that the data agrees with the model.

Figure 7.2 shows χ^2 and the corresponding EI-value for different values of L for the fit shown in figure 7.1. The minimum in χ^2 gives the value of L that best fits the data set. The fact that the minimum (normalized) χ^2 values are of the order 1 indicates that the model describes the data well.

7.1.2 Analysis of partial data sets

As a control, separate fits were performed to *parts* of the data sets. The segments were constructed by applying two distinct selection criteria on force and distance time series data of actin constructs[1]:

[1] For microtubules, not enough data sets were available to obtain reasonable statistics.

Criterion a: The data was split by selecting for *oscillation direction*: the 'straining' and 'relaxing' parts (indicated as ↑ and ↓, respectively) of the construct's oscillatory motion were split from the (synchronized) time traces as indicated in figure 7.3 and fit as separate data sets. By this means, the bead-filament-bead configuration was tested for the presence of any *hysteretic* behavior (not accounted for in the mechanical model).

Criterion b: Each data set was split into two or three consecutive *time intervals*, which were fit one by one. (These smaller intervals were in turn separated in a straining and relaxing part as in criterion a). *Degradation* of the filament or its attachment to the beads during the experiment should show up as changes in the construct's force-extension behavior.

The EI values that were obtained with these partial data set analyses were treated as individual results. All these values—both for F-actin and microtubules—are listed in tables 7.2 and 7.3 on page 65 for reference.

Figure 7.4 on the next page shows the EI fit results from all actin data split up according to criterion b). The offset parameter (figure 6.9 on page 53) often had to be slightly adjusted for each consecutive datasets due to drift in the quadrant diode (force) signal. No significant trends are observed, which is essentially a proof for constancy over time. In particular, even in cases of a construct break no changes were observed until the break event.

In figure 7.5 on the next page, results of data splitting according to criterion a) are shown. Although individual data sets may give different EI values when split by direction (see the tables on page 65), on average there is no

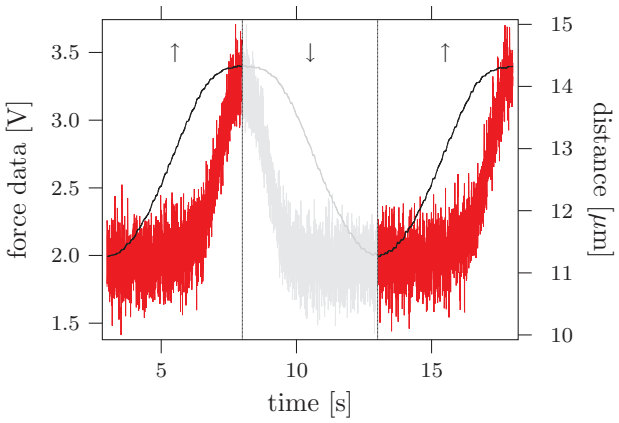

Figure 7.3: Time traces of synchonized force (noisy line) and distance for a typical actin data set, separated by oscillation direction. The straining segments of the data—that is, parts having upwards (↑) slopes—are highlighted; relaxing (↓) segments are discarded. Straining and relaxing segments are then fit separately, the results of which are in figure 7.4.

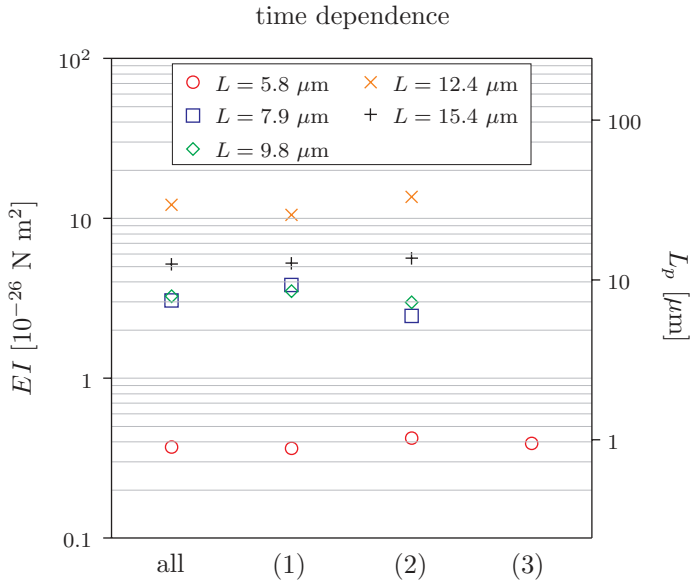

Figure 7.4: EI values (and corresponding persistence lengths, obtained with equation 2.7 on page 17) obtained from analysis of actin data sets in subsequent time intervals. A data set was divided into two or three segments and fit. No trends are observed within data sets, indicating that degradation of the filaments or their attachment to the beads, if any, influences the force-distance behavior of the constructs. The deviant data set with $L = 5.8$ μm is discussed in the text.

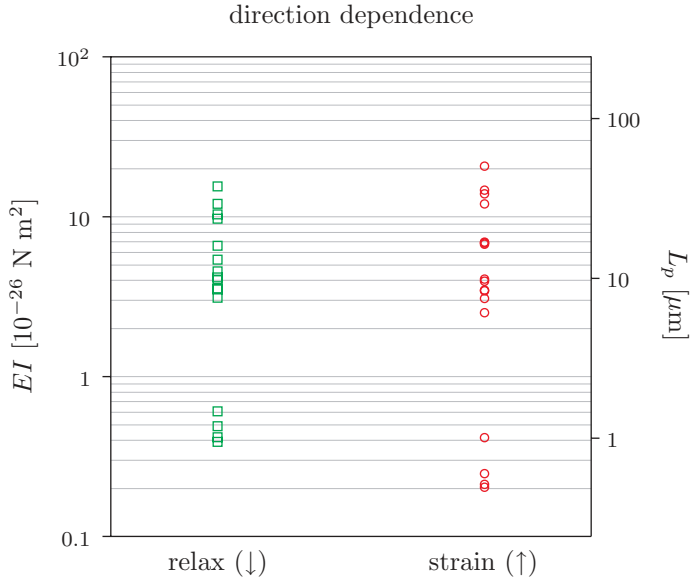

Figure 7.5: Fit EI values (and corresponding persistence lengths, obtained with equation 2.7 on page 17) obtained after separating the upwards and downwards slopes of the trap oscillation—that is, 'straining' and 'relaxing', respectively. No trends are observed within data sets, suggesting the absence of any hysteretic mechanism (not incorporated in the model).

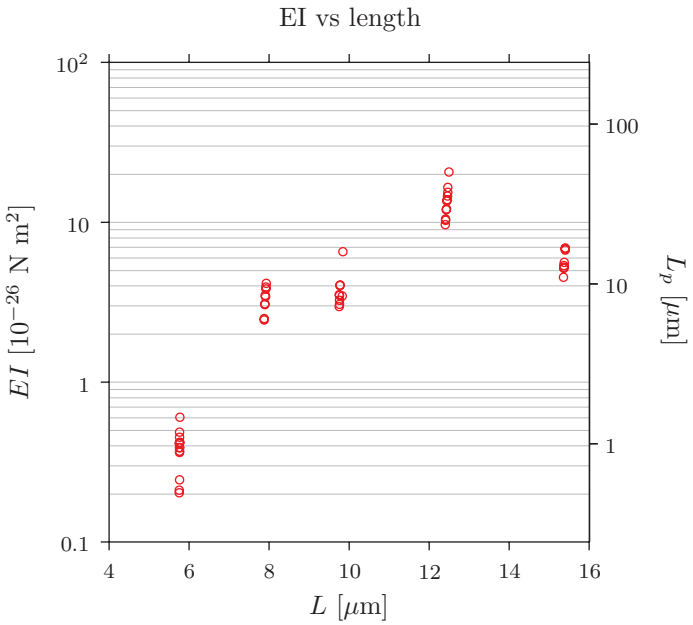

a.

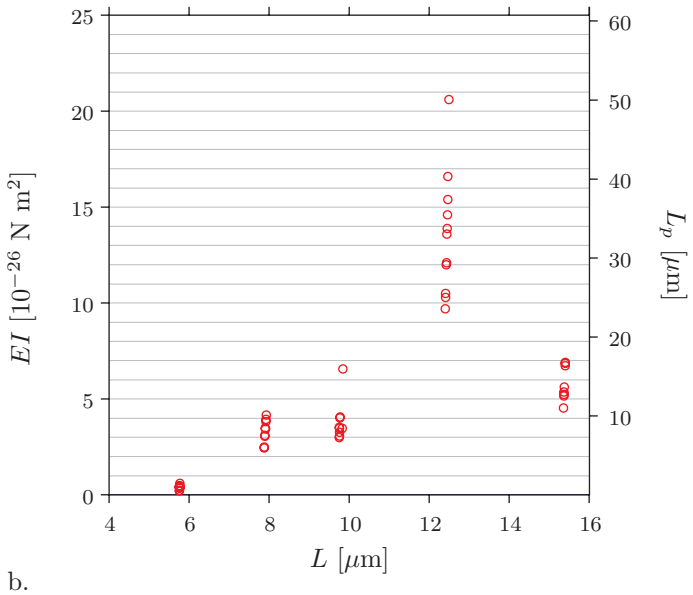

b.

Figure 7.6: Fit EI-values for F-actin as a function of filament length. The right axes show according persistence lengths, obtained with use of equation 2.7 on page 17. The values at each length were obtained in different measurements on the same construct. The logarithic plot (figure a) shows that the relative spreads within these values is roughly constant, indicating that they are merely statistical. The values for $L = 5.8$ μm were obtained from a construct with 1-μm diameter beads; all other data was taken with $D = 2.2$ μm. This data set and that with $L = 12.4$ μm deviate significantly from the other three, yet no L^2-trend as reported in [40] (see chapter 8) is observed.

distinction between increasing or decreasing strain in the construct—another indication that no unexpected hysteretic behavior seems to come into play.

7.1.3 Length dependence

As a final control, figure 7.6 shows the obtained values for the different actin constructs—including values acquired from the partial data set analyses—as a function of construct length L. The flexural rigidity is a mechanical parameter of the rod that only depends on the cross section, but not on the length. Hence, no length dependence is expected.

From this figure, as well as from the data tables on page 7.2, the data set with $L = 5.8$ μm is seen to have an EI value that is about one order of magnitude smaller than the others. Although no peculiarities like those listed on page 57 were observed in these data, this large a discrepancy seems suspicious. Moreover, the suspicion is increased by the fact that this set is unique in that 1-μm beads instead of 2.17-μm beads were used for the construct. In fact, according to *Chauvenet's criterion* (see, for example, [41]) this set should be rejected.

7.1.4 Flexural rigidity values

Upon averaging all the obtained values for the flexural rigidities of F-actin and microtubules, respectively, the final values as listed in table 7.1 are obtained. Note that the listed uncertainties are the standard deviations of the mean:

$$\sigma_{\overline{EI}} = \frac{\sigma_{EI}}{\sqrt{N}},$$

with N the number of values over which was averaged. Estimates of uncertainties in any of the fixed parameters used in the fits are hence *not* taken into account in these uncertainties. A more detailed discussion is found in chapter 8.

The table contains two averaged values for F-actin: one in which the suspicious 1-μm bead data set is included, and one excluding it.

filament	**EI**	$\mathbf{L_p}$
F-actin	$(5.4 \pm 0.7) \cdot 10^{-26}$ N m^2	13.2 ± 1.7 μm
F-actin *without* 1-μm bead	$(7.1 \pm 0.8) \cdot 10^{-26}$ N m^2	17.2 ± 1.8 μm
microtubules	$(4.2 \pm 0.4) \cdot 10^{-24}$ N m^2	1.0 ± 0.1 mm

Table 7.1: Average EI values. The indicated error margins are the statistical standard errors that do not take into account any uncertainties in the parameters that are fixed while fitting.

7.2 Attachment stiffness

As was explained in section 2.4, the bending experiments can be used to characterize the stiffness of the bead-filament-bead construct as a function of tension, which is relevant for the three bead motor assay. This stiffness is obtained as the 'Hookean' spring constant, i.e. as the derivative of force-extension curve:

$$\kappa = \frac{dF}{dX}.$$

Figure 7.7 shows this stiffness as a function of tension. Graphs are shown for F-actin and microtubules, each for two different bead sizes. The figure was obtained by differentiating the numerical results of the bending model, shown in figure 2.3 on page 16. The average[2] EI values resulting from the bending experiments (table 7.1) were used to convert the normalized forces (FD^2/EI) into physical units.

Note that actin constructs reach a certain stiffness value at lower tensions than microtubules. This might seem counterintuitive at first glance because of actin's much lower rigidity (about two orders of magnitude!). However, it is explained by the fact that actin filaments enter the non-linear range at lower forces than microtubules (as was anticipated in section 2.4).

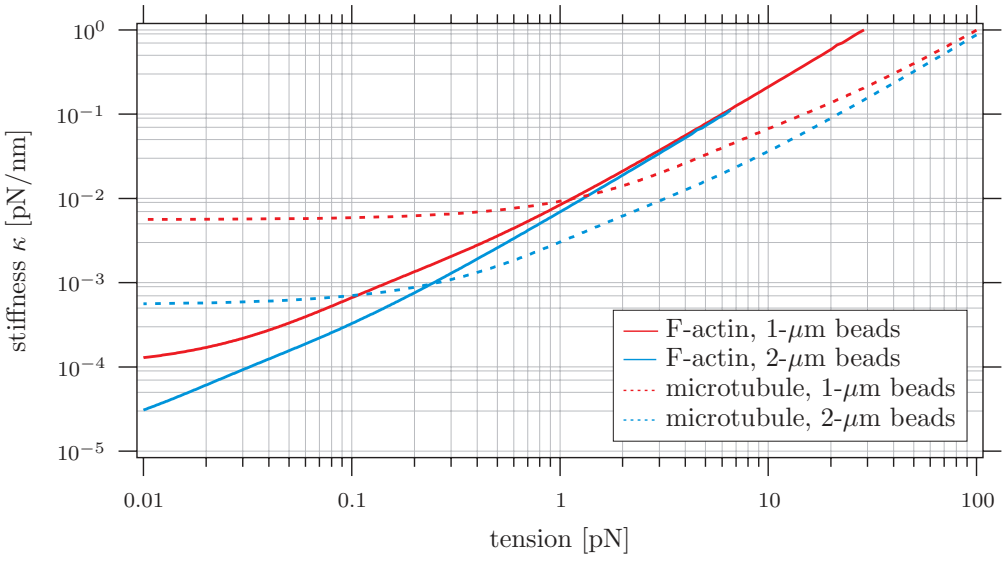

Figure 7.7: Stiffness of the bead-filament-bead construct as a function of tension, obtained by differentiating the numerical results of the bending model ($L/D = 3$; see appendix A). Curves are plot for both F-actin and microtubules, for two bead sizes. EI values as listed in table 7.1 were used in the calculations.

[2]For actin, the value $EI = 7.1 \cdot 10^{-26}$ N m^2 was used.

Table 7.2: F-actin data (EI values are in pN nm^2; lengths in μm)

data set	D		full dataset			segment 1			segment 2			segment 3		
			↑	↓	both	↑	↓	both	↑	↓	both	↑	↓	both
11-03 04	2.17	**EI**	$4.1 \cdot 10^3$	$4.9 \cdot 10^3$	$4.5 \cdot 10^3$									
		L	5.75	5.76	5.76									
11-03 05	2.17	**EI**	$2.5 \cdot 10^3$	$3.9 \cdot 10^3$	$3.7 \cdot 10^3$			$3.6 \cdot 10^3$	$2.1 \cdot 10^3$	$4.2 \cdot 10^3$	$4.2 \cdot 10^3$	$2.0 \cdot 10^3$	$6.1 \cdot 10^3$	$3.9 \cdot 10^3$
		L	5.76	5.76	5.76			5.76	5.75	5.76	5.77	5.75	5.77	5.76
14-03 05	2.17	**EI**	$3.1 \cdot 10^4$	$6.6 \cdot 10^4$	$3.3 \cdot 10^4$	$4.1 \cdot 10^4$	$4.0 \cdot 10^4$	$3.5 \cdot 10^4$	$3.5 \cdot 10^4$	$3.5 \cdot 10^4$	$3.0 \cdot 10^4$			
		L	9.76	9.84	9.76	9.77	9.77	9.76	9.82	9.75	9.75			
22-03 03	2.17	**EI**	$6.7 \cdot 10^4$	$5.4 \cdot 10^4$	$5.2 \cdot 10^4$	$6.9 \cdot 10^4$	$4.5 \cdot 10^4$	$5.3 \cdot 10^4$	$6.8 \cdot 10^4$	$4.5 \cdot 10^4$	$5.6 \cdot 10^4$			
		L	15.40	15.37	15.37	15.40	15.36	15.37	15.40	15.36	15.38			
24-03 04	2.17	**EI**	$1.4 \cdot 10^5$	$1.2 \cdot 10^5$	$1.2 \cdot 10^5$	$1.2 \cdot 10^5$	$9.7 \cdot 10^4$	$1.0 \cdot 10^5$	$1.5 \cdot 10^5$	$1.5 \cdot 10^5$	$1.4 \cdot 10^5$			
		L	12.45	12.43	12.43	12.43	12.40	12.41	12.46	12.46	12.45			
24-03 05	2.17	**EI**	$2.1 \cdot 10^5$	$1.0 \cdot 10^5$	$1.7 \cdot 10^5$									
		L	12.50	12.41	12.47									
24-03 06	2.17	**EI**	$3.4 \cdot 10^4$	$3.5 \cdot 10^4$	$3.1 \cdot 10^4$	$3.9 \cdot 10^4$	$4.2 \cdot 10^4$	$3.8 \cdot 10^4$	$2.5 \cdot 10^4$	$3.1 \cdot 10^4$	$2.4 \cdot 10^4$			
		L	7.91	7.90	7.90	7.92	7.92	7.92	7.88	7.89	7.88			

Table 7.3: Microtubule data (EI values are in pN nm^2; lengths in μm)

data set	D		full length			segment 1			segment 2			segment 3		
			↑	↓	both	↑	↓	both	↑	↓	both	↑	↓	both
23-01 08	2.17	**EI**				$2.0 \cdot 10^6$	$2.9 \cdot 10^6$	$1.9 \cdot 10^6$	$3.9 \cdot 10^6$	$5.1 \cdot 10^6$	$2.9 \cdot 10^6$	$1.8 \cdot 10^6$	$4.4 \cdot 10^6$	$2.3 \cdot 10^6$
		L				12.85	12.95	12.82	13.09	13.13	12.96	12.74	13.12	12.86
23-01 09	2.17	**EI**				$3.8 \cdot 10^6$	$6.3 \cdot 10^6$	$6.8 \cdot 10^6$	$5.6 \cdot 10^6$	$8.0 \cdot 10^6$	$5.8 \cdot 10^6$	$2.9 \cdot 10^6$	$7.1 \cdot 10^6$	$4.6 \cdot 10^6$
		L				13.04	13.20	13.24	13.22	13.28	13.20	13.02	13.24	13.12
25-01 03	2.17	**EI**	$7.2 \cdot 10^5$	$2.7 \cdot 10^6$										
		L	16.2	16.8										

CHAPTER 8

Discussion and conclusions

In this chapter, the results shown in the last chapter are discussed and compared to the literature.

8.1 Sources of error

As was mentioned in the last chapter, the uncertainties in the flexural rigidities (table 7.1 on page 63) only represent the statistical standard deviation of the mean. The true uncertainty is also influenced by other random and systematic errors. Although difficult to treat in a quantitative way, estimates of possible sources of error are given below.

8.1.1 Sensitivity to input parameters of the fit

As was described in section 6.4, the data was fit to the bending model with two fit parameters: the flexural rigidity EI and the relaxed construct length L. All other parameters—force calibration factor, quadrant diode signal (that is, force) offset, bead diameter, and pixel calibration factor—were fixed. In practice, these parameters have a finite random or, worse, systematic error. It is not possible to analytically calculate the error propagation since the exact model was integrated numerically. For the fitting of the data, an analytical interpolation formula was used (equation 6.2 on page 52) which could in principle be differentiated, but since a special procedure was used to fit to the relaxed length (see section 6.4), the error propagation was analyzed as follows.

Starting from an integrated exact numerical result (force FD^2/EI against normalized extension X), a 'fake' raw data set was reconstructed with parameters given in table 8.1. Then the input parameters were systematically varied with respect to their 'true' values. The effect of those variations on the fit

		fitted values				relative errors			
error in value		*-5%*	*-1%*	*1%*	*5%*	*-5%*	*-1%*	*1%*	*5%*
pixel	EI	4.61	5.03	5.26	5.72	7.8%	0.6%	5.2%	14.4%
calibration	L	9.45	9.89	10.11	10.55	5.5%	1.1%	1.1%	5.5%
force	EI	4.89	5.09	5.20	5.40	2.2%	1.8%	4.0%	8.0%
calibration	L	10.00	10.00	10.00	10.00	0.0%	0.0%	0.0%	0.0%
D	EI	5.18	5.15	5.14	5.11	3.6%	3.0%	2.8%	2.2%
	L	10.05	10.01	9.99	9.95	0.5%	0.1%	0.1%	0.5%
offset	EI	6.72	5.20	4.69	4.14	34%	4.0%	6.2%	17%
	L	10.02	10.00	9.99	9.99	0.2%	0.0%	0.1%	0.1%

Table 8.1: Sensitivity to uncertainties in the various parameters that were fixed in the fitting algorithm, as listed on page 53. A 'fake' raw dataset was generated with $EI = 5.00 \cdot 10^{-26}$ N m^2, $L = 10.00$ μm, 2.00 V offset, and pixel and force calibration factors equal to 1.00. The table lists the observed fit values and their relative deviations from the 'true' value upon introduction of -5, -1, 1 and 5% relative errors in the parameters. Note that the fit values for EI and L without errors in the parameters were $5.06 \cdot 10^{-26}$ N m^2 and 9.999 μm, respectively.

results for EI and L are given in table 8.1. For these parameters, the relative error was roughly preserved in the relative error of the fitted parameters. As a worst case, 5% error in the offset caused 35% error in EI. The $\pm$5% error margins were chosen as reasonable upper bounds for the bead diameter D and the pixel and force calibration factors. For the real data, the offset parameter was determined by eye from the force-distance curves. It seems to make sense to incorporate this parameter into the fitting function for future experiments, to avoid the arbitrariness of determination by eye. From repeated evaluations of the same data set choosing a new offset value each time, the reproducibility of the EI value was found to be within $\pm\,30\%$.

It should be noted that since microtubules are much stiffer than actin filaments, microtubule data, under the limited range of forces typically applied, have smaller maximum extensions ($X \lesssim 0.6$) than the actin data. Therefore, a smaller part of the full model force-extension curve is actually used to fit the data—a force > 50 pN would be needed to get an extension of $X = 0.9$! This effect may introduce a larger error in the respective fits than in the case of actin, which gets close to the maximum extension of $X = 1$ and hence has more 'features' of the model formula to fit to.

8.1.2 Model assumptions

By using a purely mechanical model to evaluate the bending experiments (see appendix A), a few assumptions are made regarding the structure of the fila-

ments and the attachment that need justification.

'Filaments are inextensible'

The model assumes the filaments to be inextensible, i.e. the stretching stiffness is thought to be infinite. In reality, the filaments have large, but finite stretch elasticities (actin: >45 pN/nm, see [25]) and microtubules about five times stiffer. However, this stiffness is so much larger than the effective filament-bead construct stiffness as shown in figure 7.7 on page 64, to which it acts in series, that it can justifiably be neglected.

'Filaments are directly bound to beads'

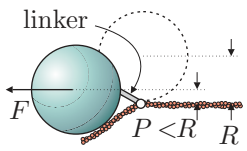

Figure 8.1: Finite linker length induces smaller lever arm R around point P.

The model assumes that the filament is attached directly to the beads. In reality, the attachment occurs via the protein *streptavidin* (see appendix B.1) and thus has a finite linker arm of about 4.5 nm, the dimensions of this 'glue' protein. This makes the attachment appear stiffer than it is, since the filament is effectively more longitudinally stretched than bent. Consider the case of a very long linker molecule as shown in figure 8.1: for increasing force, the lateral attachment of the linker has a progressively shorter lever arm around point P than in the case when the bead is attached directly onto the filament—in which case it is constant—and therefore generates a smaller bending moment. The pulling force then tends to stretch the filament more than it bends it .While this effect was difficult to quantify (as seen in the figure, a second connection point is introduced, requiring a more complicated mechanical model), it is assumed to be negligible because of the small linker molecule's dimensions.

'Microfilaments obey macromechanics'

Although the mechanical derivation of the bending model in principle holds for any cross-sectional shape of the filament (or rod), it is assumed that the cross section does not change significantly on application of bending torques. This might not always be the case for biopolymers, which consist of inhomogeneous protein structures. The proteinaceous nature of F-actin and microtubules—together with their respective helical and cylindrical structures as described in chapter 1—might hamper a description in purely mechanical terms like flexural rigidity.
It should be noted that this issue not only affects the model presented here,

but rather the use of the mechanical quantity 'flexural rigidity' applied to proteinaceous filaments in general, since it implies homogeneity along the length of the filament.

However, mechanical assumptions like these have been successfully applied to microscopic biopolymers in many experiments in the past. It seems that in the present case these assumptions are justified as long as the radius of curvature is larger than the 'typical' length scales of the filaments: the 37-nm helical repeat for actin, and the 8-nm tubulin dimer size for microtubules. From equation A.25 on page 84, an estimate of the smallest radius of curvature at high forces can be obtained. At a 10-pN stretching force, this is roughly 50 nm for actin and 350 nm for microtubules, justifying the mechanical formulation.

'Thermal effects can be neglected'

As stated above, the model is purely macromechanical. Therefore, it does not take into account the thermal forces that the filaments feel from their environment. The *worm-like chain* model, which is generally used to describe thermal bending effects for (semi-)flexible polymers [9] states that thermally induced undulations ('entropic elasticity') are eliminated by the application of a stretching force on the order of k_BT/L_p. For both F-actin and microtubules these forces are much smaller than the typical piconewton forces applied in these experiments—$2 \cdot 10^{-4}$ and $4 \cdot 10^{-6}$ pN, respectively.

'No material fatigue and hysteresis occur'

The controls that I performed on the actin data (figures 7.4 to 7.6 on pages 61–62) suggest that the model well describes the force-extension behavior of the constructs. The observation that no trend occurs over time supports the claim that no (chemical) degradation changes the construct's bending properties significantly. Moreover, the absence of hysteretic features in the longitudinally oscillated construct indicates that there is no 'memory' of the periodically applied mechanical deformations in the filament or its attachment to the beads. However, the spread that is observed within the values—in particular those obtained with 1-μm beads deviate markedly—calls for more experiments to get better statistics and a better control over some of the crucial parameters.

Altogether, the above model assumptions are justifiable. Although not precisely quantified, it is therefore not expected that significant systematic errors are introduced by these assumptions.

8.2 Comparison to literature

8.2.1 Flexural rigidities

The flexural rigidities of actin and microtubules have been investigated earlier in a variety of experiments. Tables 8.2 and 8.3 on the next page list some experimentally found values for the flexural rigidity of taxol-stabilized microtubules and rhodamine-phalloidin labeled F-actin, respectively. Corresponding persistence lengths are shown as well. As described in section 2.3, the reported values result from two types of experiments: thermal and active experiments, which is also indicated in the tables for each value.

Active versus thermal experiments

There are a few marked distinctions between active and thermal experiments. In the case of thermal experiments one often analyzes the amplitudes of thermally excited bending modes from video. Typically, only modes up to the first two orders can be considered due to low amplitudes, causing poor signal-to-noise ratios [19]. By definition, when looking at thermal fluctuations one looks at the linear response regime.

In contrast, in active experiments much higher forces are applied to the filaments usually at isolated points along their contour length. As in the present case, nonlinearities of the mechanical description can often not be neglected. Moreover, effects of local filament defects due to the concentrated application of forces are more likely to occur for active than for thermal experiments.

In the paper by Venier *et al.*, both a thermal and an active experimental protocol are described and compared. They report the two methods to yield consistent results for microtubules[1].

F-actin

The EI values reported for F-actin do not converge within less than a factor of five. The most probable reason that the values for this is the fact that very diverse experimental and theoretical approaches—each with their own assumptions and experimental errors—were used to acquire the various numbers[2]. The experimental method described in this thesis is most closely related to that of Dupuis *et al.* [13]. They derive a bending model for the same bead-filament-bead configuration, yet make the assumption of the filament bend to be localized at

[1] This comparison was carried out for microtubules that were not stabilized with taxol.

[2] Moreover, experiments in the field of biophysics typically have notoriously large error margins.

F-actin literature values

group	method	EI (10^{-26} N m^2)	L_p (μm)
Dupuis, Guilford *et al.* [13]	active	1.5 ± 0.4	3.6 ± 0.1
Riveline, Wiggins *et al.* [35]	thermal	3.0 ± 0.1	7.4 ± 0.2
Arai, Yasuda *et al.* [4]	active	5.5 ± 0.2	13.4 ± 0.5
Ott, Magnasco *et al.* [32]	thermal	6.9 ± 0.1	16.7 ± 0.2
Gittes, Mickey *et al.* [19]	thermal	7.3 ± 0.4	17.7 ± 1.1
bending experiments	active	7.1 ± 0.8	17.2 ± 1.8

Table 8.2: Experimentally found values for flexural rigidities and persistence lengths of rhodamine-phalloidin labeled (see section 4.2) actin filaments, as reported in the literature[3].

Microtubules literature values

group	method	EI (10^{-24} N m^2)	L_p (mm)
Felgner, Frank *et al.* [15]	active	1.9 ± 0.1	0.46 ± 0.02
Allersma [3]	active	4.3 ± 1.7	1.0 ± 0.4
Venier, Maggs *et al.* [43]	thermal	4.9 ± 0.4	1.2 ± 0.1
Gittes, Mickey *et al.* [19]	thermal	22 ± 1	5.2 ± 0.2
Mickey and Howard [29]	thermal	26 ± 2	6.3 ± 0.5
Dogterom and Yurke [11]	thermal	34 ± 7	8.3 ± 1.7
bending experiments	active	4.2 ± 0.4	1.0 ± 0.1

Table 8.3: Experimentally found values for flexural rigidities and persistence lengths of taxol-stabilized microtubules, as reported in the literature[3].

the beads with constant radius of curvature (i.e., with circular shape). The application of the full numerical solution of the equations for this filament bending configuration as described in this thesis yields a more precise and reliable value. Another difference with the approach described here is the protocol of attaching filaments to beads: they incubate passivated myosin proteins onto beads that bind non-reversibly to actin filaments, yet do no longer exert motor activity. Since myosin as a linker molecule is physically much larger than streptavidin, the stiffening effect described in section 8.1.2 due to the finite linker size is expected to increase. However, this effect would cause their observed rigidity to be an overestimate and therefore it does not explain their low value.

[3] In cases where EI and L_p were not *both* provided by the reference, the missing quantity was calculated with use of equation 2.7 on page 17 (inserting a 25°C room temperature).

Microtubules

The values found for microtubules appear to fall into two categories, clustered around a persistence length of 1 mm and 6 mm, respectively. The values reported in this thesis agree excellently with the results in the former category. Strikingly, table 8.3 shows that the thermal experiments almost all fall into the latter.

The microtubule values reported by Allersma *et al.* [3] were obtained in a similar way to that described here, yet with the microtubules in a *buckling* bend rather than under strain, requiring a different model for analysis. The values are in excellent agreement with those presented here.

Recently, Takasone *et al.* have reported the flexural rigidity of microtubules to vary with the individual filament's arc length as L^2 [40]. In their configuration, a microtubule was attached on one side to a glass surface and on the other to an optically trapped bead. Although not enough microtubule data is available from the bending experiments described here to refute this claim, it should be noted that their analysis fully neglects the effect of the bead being *laterally* attached to the filament. In fact, that effect is just the basis of the analysis presented here. Moreover, their configuration is not confined to the microscope's focal plane, while this is assumed in their analysis.

8.2.2 Effective stiffness for three-bead motility assays

The effective attachment stiffness of the bead-actin-bead constructs, shown in figure 7.7 on page 64 as a nonlinear function of tension, is discussed in a few articles.

Veigel *et al.* [42] deduce a measure for the attachment stiffness from the slope of a *linear* fit to (part of) a force-extension curve. This number is reported to be 0.13 pN/nm within the 1–2 pN tension range for 1.1 μm beads, which is signficantly higher than the values obtained from figure 7.7 on page 64. Most likely, this discrepancy is due to the fact that they use, like Dupuis *et al.*, passivated-myosin coated beads for actin filament attachment. Moreover, they have changed the buffer conditions to low-salt after incubation of the myosin molecules onto the beads, in which case myosin tends to *polymerize*. Therefore, their linker molecules are much longer, explaining their observed high attachment stiffness (see section 8.1.2).

Dupuis *et al.* [13] observed the nonlinearity of the stiffness after correction for the trap stiffness, which couples to the bead in series with the filament. However, they fitted this to an empirically found function. In contrast, the

model described here gives a quantitative relation between stiffness and tension, derived from a physical model, which is in reasonable quantitative agreement with their observations.

8.3 Conclusions

The experimentally found force-extension curves of the bead-filament-bead constructs that were measured with microtubules and actin filaments are in good agreement with the bending model that was introduced in chapter 2 (and mathematically derived in appendix A).

These curves have resulted in new, independent values for the flexural rigidities of these filaments, that fall within the wide range of values reported in the literature. It is likely that the bending experiments reported here are more accurate since the experimental parameters are better controlled than in most other cases.

Furthermore, the highly nonlinear stiffness behavior, induced by the lateral attachment of the filaments to the beads, makes actin filaments in these constructs appear stiffer at a certain stretching force than microtubules, although the latter are in fact much more rigid.

This observation is relevant for the three-bead assay, discussed in chapters 1 and 2 and can be directly applied in these experiments. To acquire a certain attachment stiffness, figure 7.7 on page 64 gives the required tension (depending on bead size and filament type).

The deviant EI values obtained with 1-μm beads and actin filaments call for more experiments with these constructs, since these values are based on just a single measurement.

APPENDICES

APPENDIX A

Derivation of bending model

This appendix derives the equations describing the deformation of a thin, flexible filament put under tension by two laterally attached spheres that are pulled apart.

A.1 Equilibrium equations

We start by deriving the equilibrium equations for a rod, bent by external forces. We consider an infinitesimal segment of rod of length $d\ell$. Two forces $-\mathbf{F}$ and $\mathbf{F} + d\mathbf{F}$ are supposed to act on the left and right cross sections of the segments, respectively, as a result of the internal stress that maintains the rod's shape. The change in shape is due to an external force equal to $\mathbf{K}$ *per unit length*. Then the total force acting on the segment is $d\mathbf{F} + \mathbf{K}d\ell$. In equilibrium this should be zero, yielding

$$\frac{d\mathbf{F}}{d\ell} = -\mathbf{K}. \tag{A.1}$$

Another equation is found by similar considerations for the moment of the internal forces at equilibrium. One finds (see [28]):

$$\frac{d\mathbf{M}}{d\ell} = \mathbf{F} \times \frac{d\mathbf{r}}{d\ell} \equiv \mathbf{F} \times \mathbf{t}, \tag{A.2}$$

where $\mathbf{r}$ is a vector from a fixed origin to a point along the rod and $\mathbf{t}$ a tangential unit vector along the rod at that point. For external forces acting at isolated points along the rod, $\mathbf{K} = 0$ for all other points and equations A.1 and A.2 simplify to

$$F = \text{constant} \tag{A.3}$$

and

$$\mathbf{M} = \mathbf{F} \times \mathbf{r} + \text{constant}. \tag{A.4}$$

On the other hand, it can be shown (chapter 2) that for a rod of circular cross section[1] the magnitude of the bending moment is given by

$$M = \frac{EI}{R} \tag{2.3}$$

with EI the flexural rigidity and R the radius of curvature, as described in chapter 2. This equation is known as the beam equation.

Similar results can be obtained using *energy* considerations. The bending energy of a bent rod is found to be (see [28]):

$$\mathcal{U}_{\text{bend}} = \frac{EI}{2} \int_0^L \frac{d\ell}{R^2}. \tag{A.5}$$

A.2 Boundary conditions

Let us now consider a rod bending configuration as sketched in figure A.1. The beam equation can now be written as

$$M = EI \frac{d\theta}{d\ell}. \tag{A.6}$$

With the point force F being parallel to the x-axis, equation A.4 simplifies to $M = F \cdot y$. Equating this to equation A.6 and taking the derivative ($dy/d\ell = \sin\theta$) yields:

$$EI \frac{d^2\theta}{d\ell^2} - F \sin\theta = 0. \tag{A.7}$$

The same equation can also be obtained by minimizing the total energy of the bent rod, using the bending energy from equation A.5 and the work done by the rod against the pulling force:

$$\mathcal{U} = \int_0^L d\ell \underbrace{\left\{ \frac{EI}{2} \left(\frac{d\theta}{d\ell} \right)^2 - F \cos\theta \right\}}_{u(\theta)} \tag{A.8}$$

Solving the Euler-Lagrange equations for $u(\theta)$:

$$\frac{\partial u(\theta)}{\partial \theta} - \frac{d}{d\ell} \frac{\partial u(\theta)}{\partial \dot{\theta}(\ell)} = 0,$$

we arrive at equation A.7.

Equation A.7 can be integrated once with respect to ℓ by first multiplying with $2d\theta/d\ell$ and then making use of

$$\frac{d}{d\ell} \left(\frac{d\theta}{d\ell} \right)^2 = 2 \frac{d\theta}{d\ell} \frac{d^2\theta}{d\ell^2}$$

[1] Or, more generally, a rod bent around one of its *principal axes*. See [28].

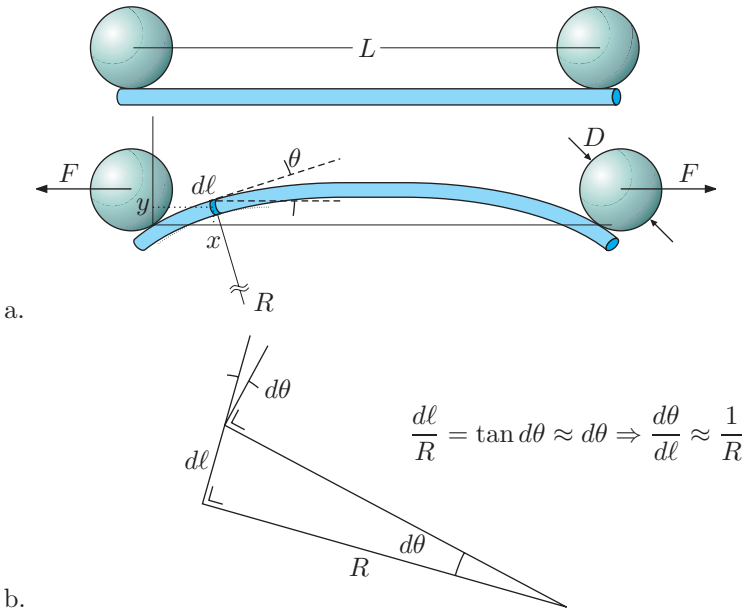

Figure A.1: Configuration of a rod of length[2] L bent by two laterally attached spheres pulled apart along the line connecting their centers by a force F. Figure a introduces the frame of reference and some relevant variables. Figure b converts the beam equation 2.3 into the new coordinates.

resulting in

$$\frac{d\theta}{d\ell} = \beta\sqrt{\mathcal{C} - 2\cos\theta}, \tag{A.9}$$

with $\beta^2 \equiv F/EI$ and $\mathcal{C}$ a constant of integration. Another integration gives

$$\beta\ell = \int_0^\theta \frac{d\theta'}{\sqrt{\mathcal{C} - 2\cos\theta'}}. \tag{A.10}$$

This can be rewritten into the form of the *elliptic integral of the first kind* (see [22], §2.571, equation 5):

$$\beta\ell = \int_0^\phi \frac{k\ d\phi'}{\sqrt{1 - k^2\sin^2\phi'}} \equiv k\mathcal{F}(\phi, k). \tag{A.11}$$

Here, the integration constant $\mathcal{C}$ has gone into the new constant k (the elliptic modulus) via

$$\mathcal{C} + 2 = \frac{4}{k^2}. \tag{A.12}$$

The integration limit ϕ depends on θ via the relations

$$\sin\phi = \frac{\sin\theta/2}{\sqrt{1 - k^2\cos^2\theta/2}} \quad \text{or} \quad \tan\phi = \frac{\tan\theta/2}{\sqrt{1 - k^2}}. \tag{A.13}$$

[2] More precisely, L is the arc length of the rod segment between the sphere attachment points rather than the full rod length.

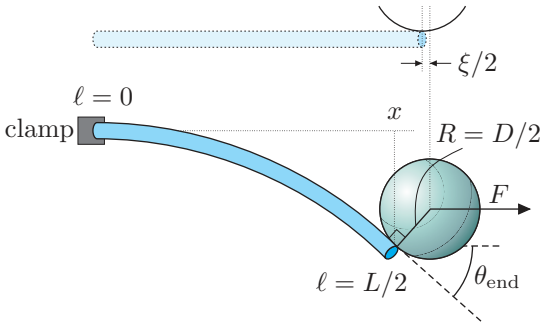

Figure A.2: Reduction of the symmetric geometry to the case where the center of the rod is clamped. The quantity ξ is the total deviation of the sphere's horizontal coordinate with respect to the 'relaxed' situation; $\xi/2$ is the deviation in this symmetric picture.

A.3 Numerical calculation

Equation A.11 describes the shape of the rod in terms of elliptic integrals. We will use these results to make a model prediction for the distance between the sphere centers and the pulling force on the spheres, as these are the quantities we can measure when our rods turn into actin filaments or microtubules, and the spheres into micrometer sized beads. The derivation and numerical analysis were done by Gittes [18].

Due to the symmetry in our configuration (figure A.1), we can simplify the problem by considering only half of the rod's length L, keeping the center of the rod *clamped*—see figure A.2[3]. The bending moment at the point where the sphere attaches to the rod is $M = FR\cos\theta_{\text{end}}$. Using equations A.6 and A.9, this can be written as

$$\beta R\cos\theta_{\text{end}} = \sqrt{\mathcal{C} - 2\cos\theta_{\text{end}}} = \frac{2}{k}\sqrt{1 - k^2\cos^2\theta_{\text{end}}/2}. \tag{A.14}$$

Via equation A.11, we can write $\beta L/2 = k\mathcal{F}(\phi_{\text{end}}, k)$. If we divide equation A.14 by this expression, we find

$$\frac{R}{L} = \frac{\sqrt{1 - k^2\cos^2\theta_{\text{end}}/2}}{k^2\mathcal{F}(\phi_{\text{end}}, k)\cos\theta_{\text{end}}}, \text{‘} \tag{A.15}$$

where ϕ_{end} is given by equation A.13. Equation A.15 enables us to find a k-value, for a fixed R/L and θ_{end}. This can be done numerically by writing

$$G(\theta) \equiv k\mathcal{F}(\phi, k)\cos\theta - \frac{L}{D}\sqrt{\mathcal{C} - 2\cos\theta} \tag{A.16}$$

[3]Note that the *anti*symmetric problem, in which the spheres are attached to the rod on opposite sides, therefore yields the same results.

and finding the roots of $G(\theta)$, using[4]

$$\frac{dG(\theta)}{d\theta} = \frac{\cos\theta - (L/D)\sin\theta}{\sqrt{\mathcal{C} - 2\cos\theta}},$$

applying the *Newton-Raphson* method for numerical root-finding and evaluating the elliptic integral $\mathcal{F}(\phi, k)$ with routines from *Numerical Recipes* [33].

This k-value can be used to get the according distance and force in the following manner. For the distance, we need the projection x of the sphere-to-rod attachment. With equations A.9 and A.11 we derive

$$\begin{aligned}\beta x &= \int_0^{L/2} \beta d\ell \cos\theta \\ &= \int_0^{\theta_{\text{end}}} \frac{d\theta \cos\theta}{\sqrt{\mathcal{C} - 2\cos\theta}} \\ &= \frac{\mathcal{C}}{2}\int_0^{\theta_{\text{end}}} \frac{d\theta}{\sqrt{\mathcal{C} - 2\cos\theta}} - \frac{1}{2}\int_0^{\theta_{\text{end}}} d\theta \frac{\mathcal{C} - 2\cos\theta}{\sqrt{\mathcal{C} - 2\cos\theta}}.\end{aligned}$$

The first term in the last line can be reduced to $\beta L/2 = k\mathcal{F}(\phi_{\text{end}}, k)$ by equations A.10–A.11. The second term can be calculated by applying another elliptic integral formula ([22], §2.576, equation 2):

$$\int_0^{\theta_{\text{end}}} d\theta \sqrt{\mathcal{C} - 2\cos\theta} = 2\sqrt{\mathcal{C} + 2}\ \mathcal{E}(\phi_{\text{end}}, k) - \frac{4\sin\theta}{\sqrt{\mathcal{C} - 2\cos\theta}} \tag{A.17}$$

with $\mathcal{E}(\phi, k)$ the *elliptic integral of the second kind*:

$$\mathcal{E}(\phi, k) \equiv \int_0^{\phi} d\phi' \sqrt{1 - k^2 \sin^2\phi'},$$

and ϕ as defined in equation A.13. We get:

$$\beta x = k\left(\frac{2}{k^2} - 1\right)\mathcal{F}(\phi_{\text{end}}, k) - \frac{2}{k}\mathcal{E}(\phi_{\text{end}}, k) + \frac{k\sin^2 2\phi_{\text{end}}}{\sqrt{1 - k^2\sin^2\phi_{\text{end}}}}. \tag{A.18}$$

We now have enough relations to find x and $\beta = \sqrt{F/EI}$ for a given θ_{end}. The total deviation of the distance between the two sphere centers from the 'relaxed' situation, ξ, now reads (see figure A.2):

$$\xi = 2x + D\sin\theta_{\text{end}}. \tag{A.19}$$

The quantities ξ and F are the measurable variables in the bending experiments performed for actin filaments and microtubules; the flexural rigidity EI of the rod is the fit parameter.

Numerical evaluation of the derived equations yields the force-extension dependence as shown in figure A.3. The curves are calculated for different values of the ratio L/D.

[4] Note that: $\dfrac{d\mathcal{F}(\phi, k)}{d\theta} = \dfrac{1}{\sqrt{\mathcal{C} - 2\cos\theta}}$.

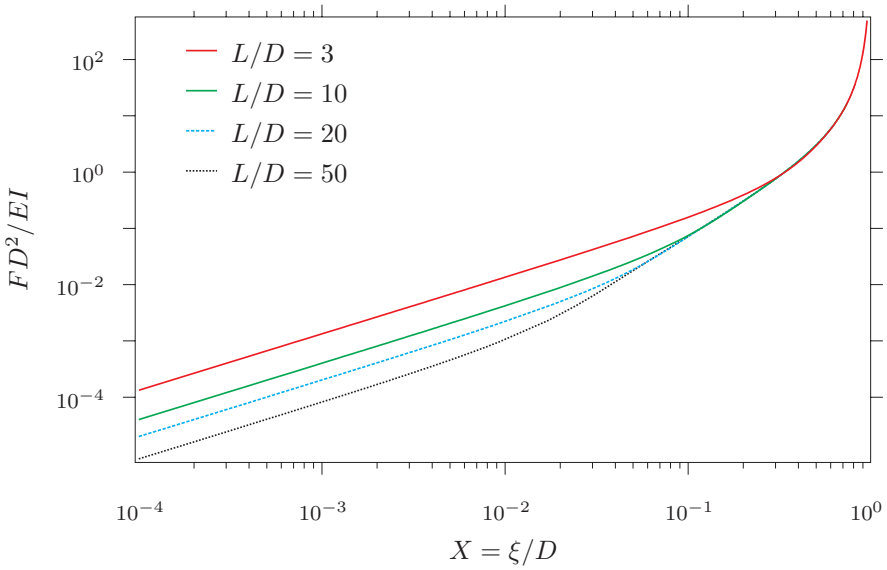

Figure A.3: Numerical results of the bending equations. Curves are shown for different values of L/D with dimensionless force and extension variables. At higher extensions, the differences between curves with different L/D ratios disappear.

A.4 Approximative analysis

The curves in figure A.3, can be divided into three segments of distinct slopes on a log-log scale. It is illustrative to treat some regimes where we can apply approximations to equation A.6 to find analytical relations between F and ξ. Figure A.4 shows three cases.

A.4.1 Weak force

For a weak force, the total change in angle $2\theta_{\text{end}} = \Delta\theta$ is small and the moment can be considered constant along the rod:

$$M \approx FR$$

yielding for the beam equation A.6:

$$FR = EI\frac{d\theta}{d\ell} \approx EI\frac{\Delta\theta}{L}. \tag{A.20}$$

The extra distance between the spheres is equal to

$$\xi = 2R\sin\theta_{\text{end}} \approx R\Delta\theta.$$

which gives a *linear* relation between force and extension:

$$F \approx \frac{EI}{LR^2}\xi. \tag{A.21}$$

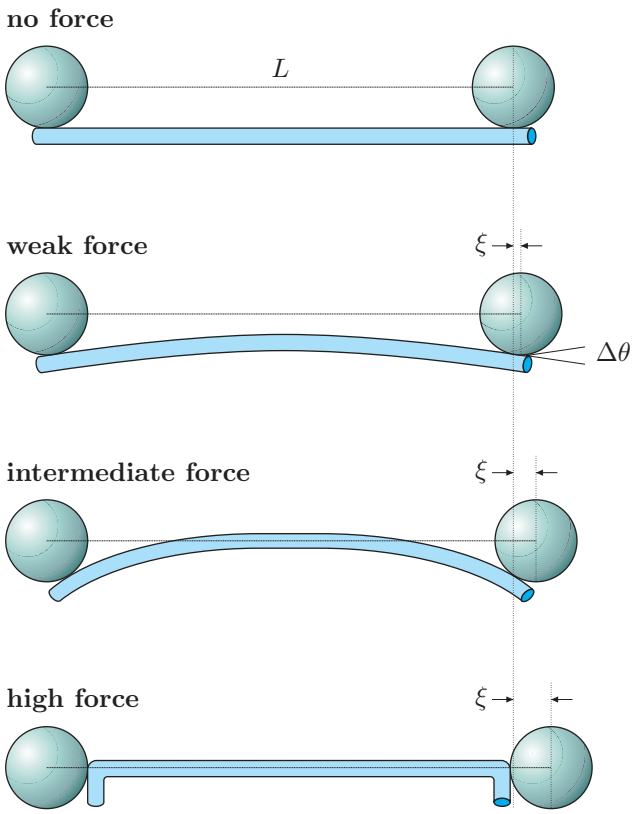

Figure A.4: Three regimes of bending force magnitude and rod shape. The top figure shows the undeformed rod with L the center-to-center distance between the spheres.

From this equation, the linear regime should be L/D-dependent, as was found in the full numerical treatment (figure A.3).

A.4.2 Intermediate force

For higher forces, the middle part of the rod will come close to the line of force. The bending angle is still considered small. Therefore, using

$$\frac{d^2y}{d\ell^2} = \frac{d\sin\theta}{d\ell} = \cos\theta\frac{d\theta}{d\ell} \approx \frac{d\theta}{d\ell},$$

the beam equation A.6 can be written in terms of the distance from the line of force, $y(\ell)$:

$$Fy(\ell) = EI\frac{d^2y}{d\ell^2}. \tag{A.22}$$

This equation gives an exponential 'decay' of the distance to the line of force away from the attachment point:

$$y(\ell) \approx R\exp\left(-|\ell-\ell_{\text{end}}|\sqrt{\frac{F}{EI}}\right), \tag{A.23}$$

$$\theta_{\text{end}} \approx \left.\frac{dy}{d\ell}\right|_{\text{end}} = R\sqrt{\frac{F}{EI}}.$$

The arc length can be calculated in a small-angle approximation [18]. Fixing the rod's length, the projection of this arc length onto the x-axis, which is shortened by the rod's bend, is obtained. Taking into account the tilt of the radius of the bead from the filament to the bead center ($R\sin\theta_{\mathrm{end}}$), which introduces an extra increase of the bead-center distance, a *quadratic* force-extension relation is obtained:

$$F \approx \frac{4}{9}\frac{EI}{R^4}\xi^2. \tag{A.24}$$

In the quadratic regime, any L/D-dependence should be absent, since only part of the rod is bent. This is in agreement with the numerical results in figure A.3.

A.4.3 High force

For high forces, the angle at the attachment point will be close to $\pi/2$ (see figure A.4). In that case, the integration constant $\mathcal{C}$ can be shown to be equal to 2, and equation A.9 becomes

$$\frac{d\theta}{d\ell} = \sqrt{\frac{2F}{EI}(1-\cos\theta)}$$

This equation can be integrated analytically [18]. The (one-sided) shortening of the x-projection of the rod-sphere attachment point due to the curvature is then found to be

$$\epsilon = \sqrt{\frac{EI}{F}}\left(2-\sqrt{2}\right). \tag{A.25}$$

The overall center-to-center distance change of the spheres ξ is

$$\xi = 2(R-\epsilon). \tag{A.26}$$

Using equations A.25 and A.26, the force-extension relation in the high-force regime becomes:

$$F \approx \frac{EI}{R^2}\left(\frac{2-\sqrt{2}}{1-\xi/2R}\right)^2. \tag{A.27}$$

An infinite force is needed for ξ to reach its maximum value, $\xi = 2R = D$. Note that also in this regime the dependence on L/D is absent, as only a small part of the rod's length is actually bent.

A.4.4 Interpolation formula

The following expression describes the force-extension dependence in the intermediate and high-force regimes and interpolates in the region between them:

$$\sqrt{\frac{FD^2}{EI}} = \frac{8}{3}X + 2\left(2-\sqrt{2}\right)\frac{X^2\sqrt{X}}{1-X}. \tag{A.28}$$

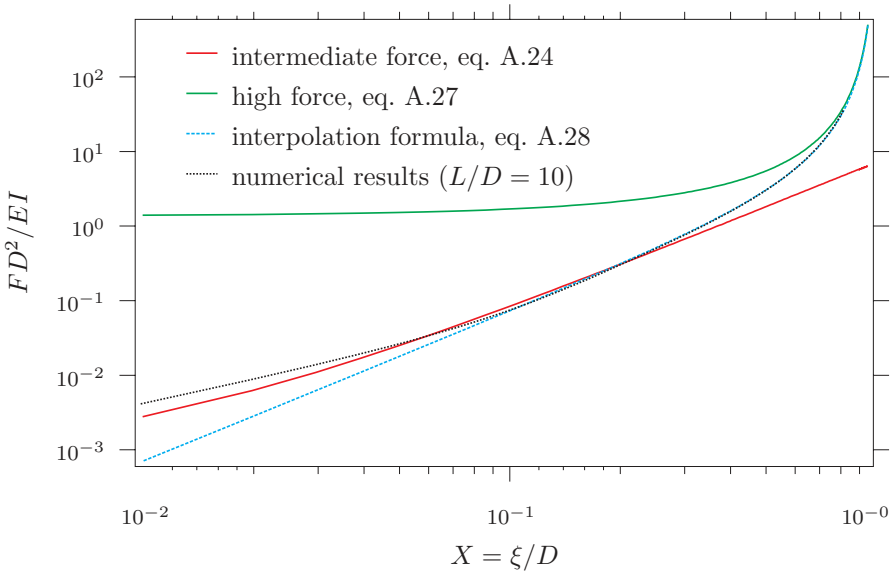

Figure A.5: Comparison of the different quantitative solutions to the bending equations—numerical results are shown for $L/D = 10$. The high and intermediate force regimes obviously depart from the numerical results outside their applicable regimes; the interpolation formula is in nice agreement with the numerical results for $X \gtrsim 0.1$.

where $X = \xi/D$ is the dimensionless deviation of the relaxed sphere distance. This expression, independent of L/D and thereby inapplicable to the linear regime, is in good quantitative agreement with the numerical results (less than 3% deviation) for $X \gtrsim 0.1$, as can be seen in figure A.5. Therefore, this equation can be used for fitting to the experimental results.

APPENDIX B

Biochemical protocols

This appendix lists the biochemical protocols that were used to obtain the microtubules and F-actin samples for the bending experiments.

B.1 Streptavidin-biotin—gluing it all together

In order to create the constructs needed for the bending experiments, the biopolymers need to be attached to the beads that are held in the optical traps. A widely applied method is the use of the protein *avidin* and its ligand *biotin*. Avidin is a *tetrameric* protein: it consists of four identical subunits, each of which has a binding site for the vitamin biotin. The avidin-biotin bond is one of the strongest non-covalent bonds known: as reported by Wong *et al.* [44], forces ranging from 90 to 400 pN are required to break it.

Streptavidin, a protein very similar to avidin, is reported to exhibit lower non-specific binding than avidin. In the bending experiments, micrometer-sized beads with a streptavidin coating—commercially available from Spherotech Inc., Libertyville, IL—where used. Biotin molecules were attached to the filaments as described below. Figure B.1 shows a cartoon (not to scale) of the attachment of beads to an actin filament via a biotin-streptavidin-biotin linker.

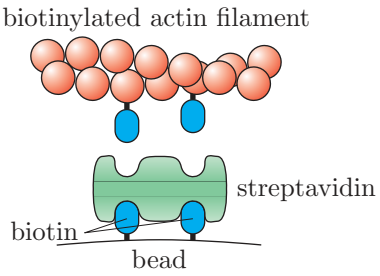

Figure B.1: Gluing filaments to beads: biotinylated (actin) filaments attach to beads that are coated with a layer of streptavidin proteins.

B.2 Microtubule preparation

Tubulin proteins were purified from bovine brain. Pure and biotinylated tubulin (catalog numbers T237 and T333, respectively, purchased from Cytoskeleton) were mixed in a 9:1 ratio and stored in 2-μl aliquots at -80°C in a buffer containing 1 mM magnesium chloride and 1 mM GTP, needed for polymerization, and glycerol.

Microtubules were polymerized after slowly thawing an aliquot and putting it on 35°C for 20-30 minutes. Next, microtubules were dilution 50× in degassed PEM80 buffer (see [3]) with 0.01 mM taxol concentration to stabilize the microtubules against depolymerization. This taxol concentration was retained throughout all further dilutions.

B.3 Actin preparation

Unlike tubulin, actin was not available in biotinylated form. The preparation of actin involved therefore three steps: production of biotinylation G-actin (non-filamentous), polymerization into filaments and fluorescent labeling with rhodamine phalloidin.

B.3.1 Actin biotinylation

The biotinylation of actin was done following a (slightly adapted) protocol by R. Rock:

- Polymerize actin with undiluted F_{10x}-buffer.
- Dilute F-actin to a total of 700 μl, and a concentration of 0.5 mg/ml.
- Distribute the actin over four Beckmann airfuge tubes.
- Spin 10 minutes at 30 psi.
- Pipette supernatant away. Add 160 μl F-buffer without DTT to each tube. Pipette a few times to dissolve pellet into solution.
- Spin 10 minutes at 30 psi.
- Pipette supernatant away. Add 160 μl F-buffer without DTT to each tube. Pipet a few times to dissolve pellet into solution. Add 4 μl of the biotin solution per tube (this is about twice the amount mentioned in Rock's protocol). Incubate for one hour at room temperature.
- Spin 10 minutes at 30 psi.

- Pipette supernatant away. Add 160 μl of F-buffer with DTT per tube.
- Spin 10 minutes at 30 psi.
- Repeat these last two steps another two times. Pipet supernatant away.
- Dissolve the four pellets into 50 μl of G_{1x}-buffer. Depolymerize overnight.
- Thaw non-biotinylated actin, mix with the labeled actin in 1:1 ratio.
- Aliquot into 2 μl aliquots in eppendorf cups. Flash-freeze in liquid nitrogen and store in -80°C.

B.3.2 Actin polymerization and labeling

Actin was polymerized at room temperature from 1:1 biotinylated:non-biotinylated G-actin by thawing a 2 μl aliquot and adding 0.2 μl F_{10x}-buffer. A first 25-fold dilution was made by addition of 50 μl of degassed F_{1x}-buffer with *anti-photobleach buffer* (see below), and 1.5 μl *rhodamine-phalloidine* to get about a 1:1 molar ratio to the actin monomers.

Another 5000-fold dilution was used for experiments. Fresh actin was prepared right before every experiment.

Anti-photobleach buffer

The anti-photobleach buffer was prepared after a recipe by Kron *et al.*[1]:

- 80 μl of degassed ddH_2O buffer;
- 10 μl of F_{10x}-buffer;
- 2 μl of glucose oxidase from 50× stock;
- 2 μl of catalase from 50× stock;
- 2 μl of glucose from 50× stock;
- 5 μl of DTT from 20× stock.

B.3.3 Sample chamber assembly

Microtubule and actin samples were diluted to obtain roughly 1–4 filaments per field of view on the camera. Streptavidin-coated beads (1.00 μm silica or 2.17 μm polystyrene, Spherotech Inc.) were added to get a likewise reasonably low density on the microscope. Sample chambers were assembled by putting two

[1] Kron, S.J. *et al.*. Methods in Enzymology, 1991, **196**: 399-416.

narrow strips of double stick tape onto a microscope cover glass and covering it with a microscope slide. Pressure was applied to ensure that the tape forms an tight seal by applying pressure. The open ends of the chamber were sealed with vacuum grease after injection of the sample to avoid flow and evaporation. Acquired sample chambers have about 20 μl volume.

APPENDIX C

Laser alignment procedure

In this appendix, I will describe the procedure of aligning the optical components in figure 6.1 on page 44 for trapping and back-focal-plane detection.

C.1 Laser and detection alignment

Figure C.1 shows the relevant optical elements for alignment. Throughout the procedure, two images are optimized: the BFP image and the image of the laser reflection on the bottom glass-water interface of the sample. It is convenient to image these planes simultaneously on two separate cameras. The procedure for aligning the AODs will be treated in a separate section.

i. Take out the telescope lenses (TL1 and TL2 in both the direct and indirect paths). Remove the beam expander (BE) from its *kinematic mount* on the platform. Mount the intermediate mirror M3′ on its kinematic mount.

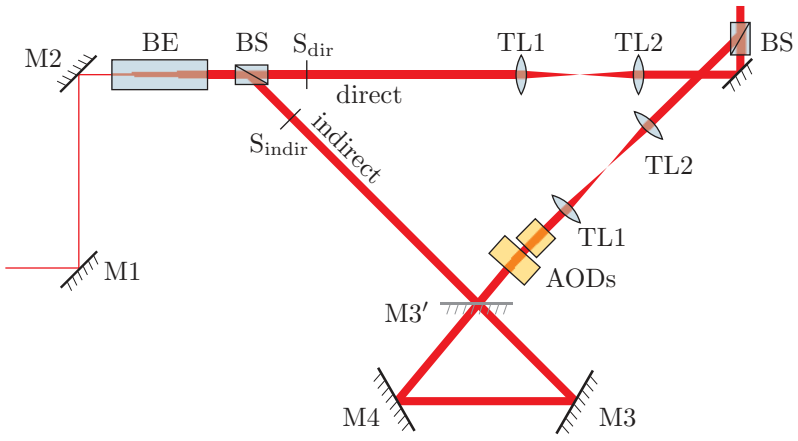

Figure C.1: Relevant optics for laser alignment. S_{dir} and S_{indir} are shutters.

ii. Focus the microscope slightly above the bottom glass-water interface of the sample.

iii. Image the BFP of the condenser lens on another camera. In the BFP, the condenser diaphragm should be in focus.

iv. Use mirrors M1 and M2 to aim the *direct* beam into the microscope. Note that:

- the beam should run parallel to the platform to enter all optic surfaces (polarizer, beam splitters, etc.) perpendicularly;
- the reflection image should be concentric with the camera's field of view and—more importantly—should not move upon focusing. The reflection should consist of concentric fringes, changing size with focus distance to the reflecting surface (see figures C.2a and b).

v. Align mirror M3′ to aim the *indirect* beam into the microscope. The orientation of the beam splitters (BS) might need slight alteration for the indirect beam to be in the horizontal plane. The reflection images of the direct and indirect beams should overlap. Note that the reflection of the indirect beam is intrinsically weaker and consists mainly of two crossing diagonal lines due to polarization effects (see figures C.2b and c).

vi. Align the condenser. First, optimize its x-y alignment until the reflection of the laser from some flat surface within the condenser overlaps with that on the bottom surface of the sample. The condenser height needs a slight adjustment in order to visualize this extra reflection. The x-y alignment screws should then be locked.

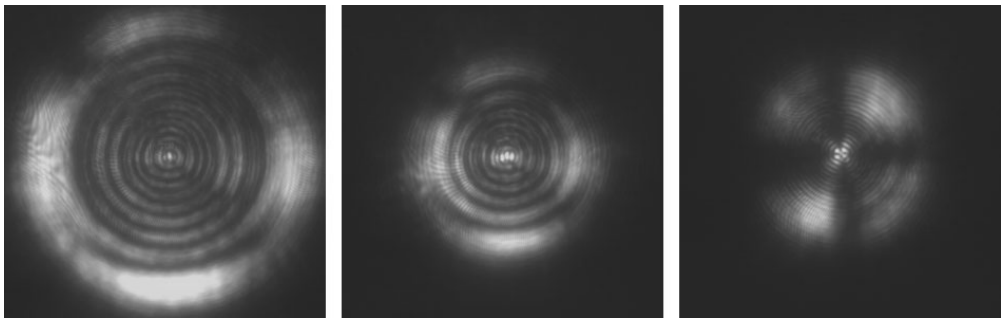

a. b. c.

Figure C.2: Reflections on the bottom glass-water interface of the sample. Figures a and b show the reflection of the direct beam for two focus depths in the sample; figure c shows the reflection of the indirect beam—note the diagonal patterns in this image, which are due to polarization effects.

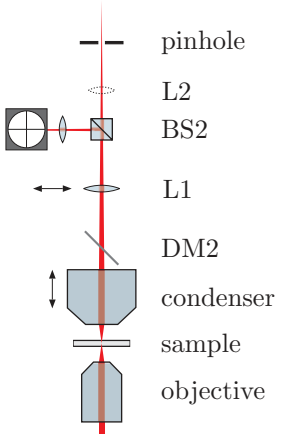

Figure C.3: Optics for the alignment of the detection path. After fixing the condenser's x-y alignment, its height needs to be adjusted to collimate the beam. The pinhole is used to aim the beam straight up, in order to have a the beam enter the splitter perpendicularly. In that way, the crosstalk between the two channels can be minimized.

vii. If needed, reinsert the beam expander (BE). Use its tilt aligner stage to touch up the BFP and reflection images of the beams. Make sure the expanded beam hits the several apertures (beam splitters, shutters, AODs, ...) in the center. It is useful to view the BFP image in *pseudo-color* for contrast enhancement.

viii. Adjust the lens before the polarizing beam splitter in the detection path (BS2) to aim the laser light through the pinhole on the top of the optical rail—note that lens L2 and the direct path quadrant detector need to be taken out. The beam will now enter the beam splitter perpendicularly, necessary for minimizing the crosstalk. Adjust the condenser-objective distance (use the condenser mount's vertical micrometer) such that a *collimated* beam enters BS2. See figure C.3.

ix. Reinsert the second telescope lens (TL2) in the direct beam path. Use its x-y alignment screws to get a homogeneous, centered Gaussian profile in the BFP. (Slowly moving circular structures in the BFP image are most likely air bubbles in the immersion oil.) Repeat for the indirect beam. Next, reinsert the first telescope lens. Check that moving the first telescope lens in the x-y plane does not or hardly change the BFP-image.
Note that in order to view the indirect beam's BFP image on a camera in the direct beam's path, a $\lambda/2$ waveplate can be used to rotate the polarization before entering the beam splitter.

x. Reinstate lens L2 such that it forms a focus at its focal length (in both the direct and indirect paths). Place the two quadrant diodes well behind this focus. The detectors should image the condenser's back focal plane, which can be checked by looking for a sharp image of the condenser's back focal plane iris.

xi. Finally, alter the x-y alignment screws of the two quadrant diodes to zero the horizontal and vertical displacement signals (see section 6.1.3) at 0 V.

C.2 AOD alignment

This section describes the alignment procedure of the acousto-optic deflectors, (IntraAction, model DTD-276HB6). As mentioned in section 5.2, the main goal during alignment of the AODs is stabilizing the power of the diffraction order (1,1) over a large enough frequency band ($\lesssim$1 octave). The AOD manual gives an adequate description of the testing and alignment procedure. However, I developed some setup arrangements and LabVIEW software to facilitate the procedure.

i. Feed both AODs with a 26 MHz acoustic frequency—the center frequency of the power stable bandwidth.

ii. Remove mirror M3′ and the telescope lenses in the indirect path.

iii. Use mirrors M3 and M4 (see figure C.1) to aim the (1,1) diffraction order into the microscope. It might be useful to put pinholes in the telescope lens holders to facilitate this. To identify the (1,1) order, it can be useful to oscillate the RF signal around 26 MHz with a very small amplitude ($\sim$0.1 MHz) in both directions. The (1,1) order should then move diagonally. Use the reflection image to center the beam at its original location.

iv. Reinsert the telescope lenses, following step (ix) in the previous section.

v. Insert a quadrant diode near—but not at—the focus of the first telescope lens TL1. Make sure a heat-absorbing filter protects the diode against the strong laser light. Use a modified pre-amplifier RIS-86 that **disables the addition** of signals of two quadrants[1]. Measure the four quadrant signals by using the X+, X–, Y+ and Y– outputs of the normalizing differential amplifier. Make sure the readouts are smaller than $\sim$1% of the [-10V...+10V] detector range by reducing the laser power, as the laser beam is very narrow and can damage the quadrant diode easily.

vi. Align this quadrant diode such that the undiffracted (0,0) beam falls at the right-bottom edge of the top-left quadrant. The other quadrants should now measure the (0,1), (1,0) and (1,1) order intensities. See figure C.4.

[1]That is, disconnect resistors **R15**, **R18**, **R27** and **R33** on board B. See the diagram of the RIS-86 pre-amplifier. One of these should be available.

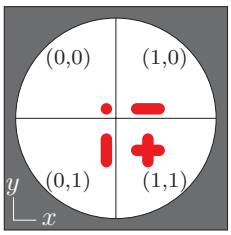

Figure C.4: Arrangement of diffracted beams on the quadrant diode. Beam responses are shown for an x-y sweep as shown in figure C.5. Only the (1,1) beam can be moved in two directions.

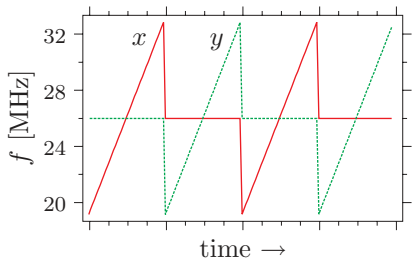

Figure C.5: Typical RF driving frequencies for alignment. First the one deflector is sweeped through its stable bandwidth while the other is kept at 26 MHz, then vice versa.

vii. Sweep the RF signal through the stable bandwidth (approximately 19 to 33 MHz). Alternate a sweep of the vertical AOD with one of the horizontal one, while keeping the other fixed at 26 MHz. See figure C.5. By recording the signals from the four quadrants, the stability of the (1,1) order can be tuned and compared to the other diffraction orders.

viii. Adjust the Bragg angles of both deflectors to optimize the total (1,1) diffraction efficiency. Use the measures for horizontal and vertical efficiency as given by equations 5.5 and 5.6.

ix. Adjust the other angles of both deflectors (orthogonal to the deflection direction) to optimize the maximum efficiency.

x. Fine tune the amplitude of the RF signal for maximum stability and flatness.

Note that some LabVIEW programs are available—both for AOD driving and quadrant diode detection—to facilitate the procedure described in this section:

- '`AOD manual align.vi`' for changing both AOD frequencies with a computer's mouse or keyboard; program can also perform oscillations around this value;
- '`AOD align periodic signal.vi`' for driving one of the AODs in a periodic fashion, i.e. with a sinusoidal, triangular, square, linear ramp or random signal;
- '`AOD align sweep X-Y.vi`' for performing the x-y sweeping as described in the aligning procedure;

- '`ChicoPlus AOD alignment.vi`' for sampling intensities from the individual segments of the quadrant diode during alignment.

There is also a compiled C-program called '`aod.exe`', which generates a square wave at up to a few kHz frequency, to be used for timeshared optical traps.

Bibliography

[1] Agayan., R.R., Gittes, F., Kopelman, R., and Schmidt, C.F. 2002. *Optical trapping near resonance absorption.* Applied Optics **41**: 2318-2327.

[2] Allersma, M.W, Gittes, F., deCastro, M.J., Stewart, R.J., and Schmidt, C.F. 1998. *Two-dimensional tracking of ncd motility by back focal place interferometry.* Biophysical Journal **74**: 1074-1085.

[3] Allersma, M.W. 2000. *Motor protein and microtubule mechanics: application of a novel high-resolution optical trapping technique.* Dissertation from the University of Michigan, Ann Arbor, MI.

[4] Arai, Y., Yasuda, R., Akashi, K., Harada, Y., Miyata, H., Konishita, K., and Itoh, H. 1999. *Tying a molecular knot with optical tweezers.* Nature **399**: 446-448.

[5] Ashkin, A. 1970. *Acceleration and trapping of particles by radiation pressure.* Physical Review Letters **24**: 156-159.

[6] Ashkin, A., Dziedzic, J.M., Bjorkholm, J.E., and Chu, S. 1986. *Observation of a single-beam gradient force optical trap for dielectric particles.* Optics Letters **11**: 288-290.

[7] Ashkin, A. 1992. *Forces of a single-beam gradient laser trap on a dielectric sphere in the ray optics regime.* Biophysical Journal **61**: 569-582.

[8] Brown, B.A., and Brown, P.R. 2001. *Optical tweezers: theory and current applications.* American Laboratory Articles, November issue, 13-20.

[9] Bustamante, C., Marko, J.F., Siggia, E.D., and Smith, S. 1994. *Entropic elasticity of λ-phage DNA.* Science **265**: 1599-1560.

[10] Davidson, M.W. and Abramowitz, M. 1999. *Optical Microscopy.* Online PDF-resource.
See also the *Microscopy Primer* at `http://micro.magnet.fsu.edu/primer`.

[11] Dogterom, M. and Yurke, B. 1997. *Measurement of the force-velocity relation for growing microtubules.* Science **278**: 856-860.

[12] Doi, M. and Edwards, S.F. 1986. *The Theory of Polymer Dynamics.* Clarendon Press, Oxford.

[13] Dupuis, D.E., Guilford, W.H., Wu, J., and Warshaw, D.M. 1997. *Actin filament mechanics in the laser trap.* Journal of Muscle Research and Cell Motility **18**: 17-30.

[14] Elliott, A. and Offer, G. 1978. *Shape and flexibility of the myosin molecule.* Journal of Molecular Biology **123**: 505-519.

[15] Felgner, H., Frank R., and Schliwa, M. 1996. *Flexural rigidity of microtubules measured with the use of optical tweezers.* Journal of Cell Science **109**: 509-516.

[16] Feynman, R.P., Leighton, R.B., and Sands, M.L. 1989. *The Feynman Lectures on Physics, volume II.* Addison-Wesley Publishing Inc., Reading, MA.

[17] Finer, J.T., Simmon, R.M., and Spudich, J.A. 1994. *Single myosin molecule mechanics: piconewton forces and nanometre steps.* Nature **386**: 113-119.

[18] Gittes, F. Private communication.

[19] Gittes, F., Mickey, B., Nettleton, J., and Howard, J. 1993. *Flexural rigidity of microtubules and actin filaments measured from thermal fluctuations in shape.* Journal of Cell Biology **120**: 923-934.

[20] Gittes, F. and Schmidt, C.F. 1998. *Signals and noise in micromechanical measurements.* Methods in Cell Biology **55**: 129-156. Book chapter.

[21] Gittes, F. and Schmidt, C.F. 1998. *Interference model for back-focal-plane displacement detection in optical tweezers.* Optics Letters **23**: 7-9.

[22] Gradshteyn, I.S. and Ryzhik, I.M. 1980. *Table of integrals, series and products* (4th edition). Academic Press Inc., New York.

[23] Hecht, E. and Zajac, A. 1987. *Optics* (2nd edition). Addison-Wesley Publishing Inc., Reading, MA.

[24] Howard, J. 2001. *Mechanics of Motor Proteins and the Cytoskeleton.* Sinauer Associates Inc., Sunderland.

[25] Janmey, P.A., Tang, J.X., and Schmidt, C.F. 1999. *Actin filaments.* Online PDF-resource from 'Biophysics Textbook online'.
Available at: `http://www.biophysics.org/btol/supramol.html`.

[26] Keeton, W.T. and Gould, J.L. 1986. *Biological Science* (4th edition). W.W. Norton and Company, New York/London.

[27] Klein, W.R. and Cook, B.D. 1967. *Unified approach to ultrasonic light diffraction.* IEEE Transactions on Sonics and Ultrasonics **SU-14**: 123-134.

[28] Landau, L.D. and Lifshitz, E.M. 1970. *Course of Theoretical Physics, volume 7: Theory of Elasticity* (2nd edition). Pergamon Press Ltd., Oxford.

[29] Mickey, B. and Howard, J. 1995. *Rigidity of microtubules is increased by stabilizing agents.* Journal of Cell Biology **130**: 909-17.

[30] National Instruments Corporation. 2000. *IMAQ Vision Concepts Manual.* Online PDF-resource.
See the NI website: `http://www.ni.com/pdf/manuals/322913a.pdf`.

[31] Nogales, E., Wolf, S.G., Downing, K.H. 1998. *Structure of the $\alpha\beta$ tubulin dimer by electron crystallography.* Nature **391**: 199-203.

[32] Ott, A., Magnasco, M., Simon, A., and Libchaber, A. 1993. *Measurement of the persistence length of polymerized actin using fluorescence microscopy.* Physical Review E **48**: R1642-R1645.

[33] Press, W.H., Teukolsky, S.A., Vetterling, W.T., and Flannery, B.P. 1996. *Numerical Recipes in C* (2nd edition). Cambridge University Press, Cambridge, MA.

[34] Reif, F. 1965. *Fundamentals of statistical and thermal physics.* McGraw-Hill Ltd., Tokyo.

[35] Riveline, D., Wiggins, C.H., Goldstein, R.E., and Ott, A. 1997. *Elastohydrodynamic study of actin filaments using fluorescence microscopy.* Physical Review E **56**: R1330-R1333.

[36] Roosen, G. and Imbert, C. 1976. *Optical levitation by means of 2 horizontal laser beams—theoretical and experimental study.* Physics Letters **59A**: 6-8.

[37] Sapriel, J. 1979. *Acousto-optics.* John Wiley & Sons, New York.

[38] Stryer, L. 1995. *Biochemistry* (4th edition). W.H. Freeman and Company, New York.

[39] Svoboda, K. and Block, S.M. 1994. *Biological applications of optical forces.* Annual review of Biophysics and Biomolecular Structure **23**: 247-285.

[40] Takasone, T., Juodkazis, S., Kawagishi, Y., Yamaguchi, A., Matsuo, S., Sakakibara, H., Nakayama, H., and Misawa, H. 2002. *Flexural rigidity of a single microtubule.* Japanese Journal of Applied Physics **41**: 3015-3019.

[41] Taylor, J.R. 1982. *An introduction to error analysis—The study of uncertainties in physical measurements.* University Science Books, Mill Valley, CA.

[42] Veigel, C., Bartoo, M.L., White, D.C.S., Sparrow, J.C., and Molloy, J.E. 1998. *The stiffness of rabbit skeletal muscle actomyosin cross-bridges determined with an optical tweezers transducer.* Biophysical Journal **75**: 1424-1438.

[43] Venier, P., Maggs, A.C, Carlier, M-F., and Pantaloni, D. 1994. *Analysis of microtubule rigidity using hydrodynamic flow and thermal fluctuations.* Journal of Biological Chemistry **269**: 13353-13360.

[44] Wong, J., Chilkoti, A., and Moy, V.T. 1999. *Direct force measurements of the streptavidin-biotin interaction.* Biomolecular Engineering **16**: 45-55.

[45] Xu, J. and Stroud, R. 1992. *Acousto-optic Devices: Principles, Design and Applications.* John Wiley & Sons, New York.